A CS $J = 5 \rightarrow 4$ MAPPING SURVEY TOWARD HIGH-MASS STAR-FORMING CORES ASSOCIATED WITH WATER MASERS

Yancy L. Shirley,[1] Neal J. Evans II, Kaisa E. Young, Claudia Knez, and Daniel T. Jaffe

Department of Astronomy, The University of Texas at Austin, 1 University Station C1400, Austin, TX 78712-1083; yshirley@aoc.nrao.edu, nje@astro.as.utexas.edu, kaisa@astro.as.utexas.edu, claudia@astro.as.utexas.edu, dtj@astro.as.utexas.edu

ABSTRACT

We have mapped 63 regions forming high-mass stars in CS $J = 5 \rightarrow 4$ using the CSO. The CS peak position was observed in $C^{34}S$ $J = 5 \rightarrow 4$ toward 57 cores and in ^{13}CS $J = 5 \rightarrow 4$ toward the nine brightest cores. The sample is a subset of a sample originally selected toward water masers; the selection on maser sources should favor sources in an early stage of evolution. The cores are located in the first and second Galactic quadrants with an average distance of 5.3 ± 3.7 kpc and were well detected with a median peak signal-to-noise ratio in the integrated intensity of 40. The integrated intensity of CS $J = 5 \rightarrow 4$ correlates very well with the dust continuum emission at 350 μm. For 57 sufficiently isolated cores, a well-defined angular size (FWHM) was determined. The core radius (R_{CS}), aspect ratio [$(a/b)_{obs}$], virial mass (M_{vir}), surface density (Σ), and the luminosity in the CS $J = 5 \rightarrow 4$ line ($L(CS54)$) are calculated. The distributions of size, virial mass, surface density, and luminosity are all peaked with a few cores skewed toward much larger values than the mean. The median values, $\mu_{1/2}$, are as follows: $\mu_{1/2}$ (R_{CS}) = 0.32 pc, $\mu_{1/2}$ ($(a/b)_{obs}$) = 1.20, $\mu_{1/2}$ (M_{vir}) = 920 $M_{\odot}$, $\mu_{1/2}$ (Σ) = 0.60 g cm^{-2}, $\mu_{1/2}$ ($L(CS54)$) = 1.9×10^{-2} $L_{\odot}$, and $\mu_{1/2}$ (L_{bol}/M_{vir}) = 165 $(L/M)_{\odot}$. We find a weak correlation between $C^{34}S$ line width and size, consistent with $\Delta v \sim R^{0.3}$. The line widths are much higher than would be predicted by the usual relations between line width and size determined from regions of lower mass. These regions are very turbulent. The derived virial mass agrees within a factor of 2–3 with mass estimates from dust emission at 350 μm after corrections for the density structure are accounted for. The resulting cumulative mass spectrum of cores above 1000 $M_{\odot}$ can be approximated by a power law with a slope of about -0.9, steeper than that of clouds measured with tracers of lower density gas and close to that for the total masses of stars in OB associations. The median turbulent pressures are comparable to those in UCH II regions, and the pressures at small radii are similar to those in hypercompact H II regions ($P/k \sim 10^{10}$ K cm^{-3}). The filling factors for dense gas are substantial, and the median abundance of CS is about 10^{-9}. The ratio of bolometric luminosity to virial mass is much higher than the value found for molecular clouds as a whole, and the correlation of luminosity with mass is tighter.

Subject headings: dust, extinction — ISM: clouds — ISM: molecules — stars: formation

1. INTRODUCTION

Many, possibly most, stars form in clustered environments with massive stars (see Carpenter 2000). Regions forming massive stars are the only detectable manifestations of star formation in other galaxies. Understanding the formation of massive stars is crucial to an improved understanding of galaxy formation. Despite all these motivations, our understanding of the conditions in which massive stars form is quite primitive. In contrast to the well-developed theories for isolated, low-mass star formation (e.g., Shu, Adams, & Lizano 1987), theories dealing with massive star formation are less developed. While promising theoretical work has been done (e.g., Bonnell et al. 1997; Bonnell, Bate, & Zinnecker 1998; Klessen 2001; McKee & Tan 2002, 2003), the theoreticians are hampered by a lack of systematic information on the properties of the regions. Many detailed observational studies of individual regions have been made, but the field has lacked statistical information based on large samples analyzed with uniform methods.

One approach to this problem has been to collect a unified database for a well-characterized sample. Most work of this kind has focused on samples selected to have ultracompact H II regions or *IRAS* colors similar to those of cores with UCH II regions (Wood & Churchwell 1989a, 1989b; Sridharan et al. 2002). The sample studied by Sridharan et al. and Beuther et al. (2002) used *IRAS* colors, but then selected against H II regions by choosing sources with low emission in the radio continuum in an attempt to identify early phases. We have sought to study an early phase by selecting sources based on their water maser emission (Cesaroni et al. 1988). A survey of a large sample of water masers revealed that emission in the CS $J = 7 \rightarrow 6$ transition was common in this sample (Plume, Jaffe, & Evans 1992, hereafter Paper I). Detection of this highly excited line suggested high densities and temperatures, but additional transitions were needed to pin down the conditions. A multitransition study of CS lines showed that the density, $n(\text{cm}^{-3})$, of the sample of 71 sources was characterized by $\langle \log n \rangle = 5.9$ (Plume et al. 1997, hereafter Paper II). That study also made cross scans of 25 sources to estimate sizes, masses, and star formation activities, indicated by the luminosity-to-mass ratio (L_{bol}/M_{vir}), where the mass referred to the dense gas probed by CS.

In the current paper, we present fully sampled maps in the CS $J = 5 \rightarrow 4$ line of many more sources (63) than were mapped in Paper II. These data should provide a much firmer statistical foundation for determining the conditions

at early stages of the formation of massive stars. We have made similar maps of CS $J = 7 \rightarrow 6$ and dust continuum emission for a subset of these sources. These data will allow a more detailed analysis of the density and temperature gradients, similar to that accomplished by van der Tak et al. (2000) on a small subset of these sources. The analysis of the dust continuum data (Mueller et al. 2002b) and combined models of CS excitation will be presented separately. While there is a wealth of information on velocity structure in this data set, we focus on the integrated intensity maps in this paper. For an example of interesting velocity structure in the S235 region, see Lee et al. (2002). A summary of early results of this work can be found in Evans et al. (2002), Shirley, Evans, & Rawlings (2002a), Shirley et al. (2002b), Mueller et al. (2002a), Knez et al. (2002), and Lee et al. (2002).

2. SOURCES AND OBSERVATIONS

Sixty-three high-mass star-forming cores (typically $M_{\rm vir} > 50\ M_\odot$) were mapped in the CS $J = 5 \rightarrow 4$ transition between 1996 September and 1999 July at the Caltech Submillimeter Telescope (CSO). Fifty-seven cores were observed in the $C^{34}S\ J = 5 \rightarrow 4$ transition, and nine cores were observed in the $^{13}CS\ J = 5 \rightarrow 4$ transition toward the $C^{32}S$ peak position between 2001 July and 2002 June at the CSO. We employ the conventional notation that, unless noted otherwise, the isotope is the most common one: thus, CS means $^{12}C^{32}S$.

2.1. The Sample

All of the objects observed are listed in Table 1. Nearly all of the cores are located in the first and second quadrant (Fig. 1). Sources were selected from Paper I and Paper II based on the strength of their CS $J = 7 \rightarrow 6$ emission with each source detected at the 1 K T_R^* level (Paper I). Within this criterion, we made some effort to include sources with weaker emission. This sample extends the sample of 25 cores mapped in Paper II by including less massive cores and fully mapping each core. The center of each map was the water maser position from the catalog of Cesaroni et al. (1988).

The sources were distributed from 0.7 to 15.6 kpc from the Sun (Fig. 1). The distances were determined from an extensive literature search (see Table 1 for distance references). Photometric distances were used whenever possible, but distance estimates to many cores are based on kinematical distances using the rotation curve of Fich, Blitz, & Stark (1989). The average distance of the sample of 63 cores is 5.3 ± 3.7 kpc, while the median distance is 4.0 kpc. The distribution is strongly peaked between 2 to 4 kpc. The sources at large distances from us are all in the first quadrant. The distances can be converted into galactocentric distances, D_g, using a distance of 8.5 kpc to the solar circle. The result is an average distance of 7.3 ± 2.6 kpc and a median distance of 6.8 kpc from the Galactic center. Most (64%) of the cores are located between 5 and 10 kpc from the Galactic center, 25% of the cores are less than 5 kpc from the Galactic center, and 11% are beyond 10 kpc (Fig. 1). This sample is characterized by regions near the solar galactocentric distance within the Galaxy.

There is very little overlap of previous CS studies ($J_u \geq 2$) selected toward water maser positions: three sources in common (Zinchenko et al. 1994); zero sources in common (Zinchenko, Mattila, & Toriseva 1995); zero sources in common (Juvela 1996); and eight sources in common (Zinchenko, Pirogov, & Toriseva 1998). There is slightly more overlap of sources selected toward UCH II regions or IRAS colors indicative of UCH II regions: 24 sources in common (Bronfman, Nyman, & May 1996); six sources
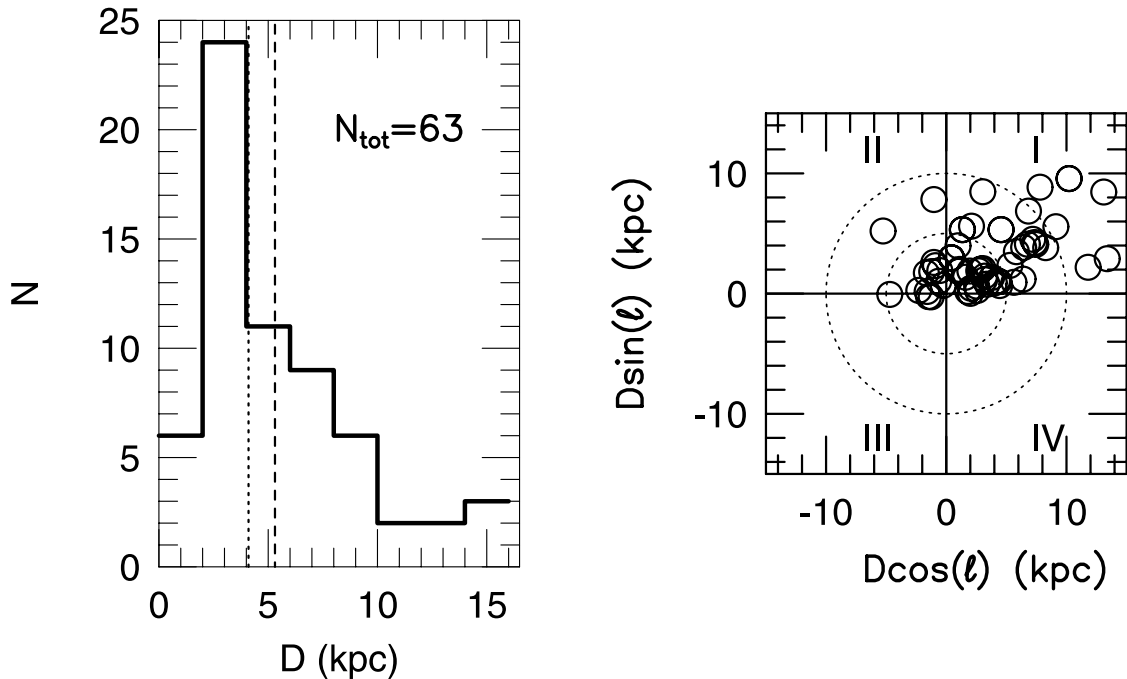
Fig. 1.—Histogram of distances and the position of the 63 mapped cores in the Galactic plane. The histogram is binned at 2 kpc. The median (dotted line) and mean (dashed line) are shown. In the Galactic coordinates plot, the Sun is at the center. Since the observations were performed at the CSO in the northern hemisphere, almost all of the cores are in the first and second quadrant. The circles represent distances of 5 and 10 kpc from the Sun.

TABLE 1
OBSERVED SOURCES

Source	α (B1950.0)	δ (B1950.0)	Date CS Mapped	Dist. (kpc)	Dist. Ref.	D_g (kpc)	H II?	H II $R_{2\,cm}$ (pc)	Size Ref.
G121.30+0.66.................	00 33 53.3	+63 12 32	1997 Dec	1.2	1	9.2	. . .	. . .	
G123.07−6.31.................	00 49 29.2	+56 17 36	1997 Dec	2.2	2	9.9	H II	. . .	
W3 (OH)..........................	02 23 17.3	+61 38 58	1996 Dec	2.4	3	10.3	UCH II	0.02	18
G135.28+2.80.................	02 39 31.0	+62 44 16	1997 Dec	7.4	1	14.7	. . .	. . .	
S231	05 35 51.3	+35 44 16	1996 Dec	2.3	2	10.8	. . .	. . .	
S235	05 37 31.8	+35 40 18	1996 Dec	1.6	2	10.1	H II	. . .	
S241	06 00 40.9	+30 14 54	1997 Dec	4.7	2	13.2	. . .	. . .	
S252A	06 05 36.5	+20 39 34	1997 Dec	1.5	2	10.0	H II	. . .	
S255	06 09 58.3	+18 00 12	1996 Dec	1.3	4	9.8	UCH II	0.01	19
RCW 142	17 47 04.5	−28 53 42	1997 Apr	2.0	5	6.5	UCH II	. . .	
W28A2 (1)	17 57 26.8	−24 03 54	1996 Sep	2.6	5, 6	5.9	UCH II	0.05	14
M8E................................	18 01 49.1	−24 26 57	1997 Apr	1.8	2	6.7	UCH II	. . .	
G9.62+0.10	18 03 16.0	−20 32 01	1996 Sep	7.0	7	3.0	UCH II	0.02	19
G8.67−0.36.....................	18 03 18.6	−21 37 59	1997 Apr	8.5	8	4.1	UCH II	0.03	14
W31	18 05 40.4	−19 52 21	1996 Sep	12.0	4	4.0	UCH II	0.05	20
G10.6−0.4	18 07 30.7	−19 56 28	1996 Sep	6.5	9	2.4	CH II	0.06	14
G12.42+0.50...................	18 07 56.4	−17 56 37	1997 Apr	2.1	10	6.5	UCH II	0.01	21
G12.89+0.49...................	18 08 56.3	−17 53 09	1997 Apr	3.5	8	5.1	. . .	. . .	
G12.2−0.1	18 09 43.7	−18 25 09	1996 Sep	16.3	11	5.7	CH II	0.27	14
W33 cont	18 11 18.3	−17 56 21	1996 Oct	4.1	9	4.6	UCH II	. . .	
G13.87+0.28...................	18 11 41.5	−16 16 34	1998 Jul	4.4	12	4.4	H II	0.41	20
W33A	18 11 44.0	−17 53 09	1997 Apr	4.5	5	4.2	. . .	. . .	
G14.33−0.64...................	18 16 00.8	−16 49 06	1997 Apr	2.6	8	6.0	UCH II	. . .	
G19.61−0.23...................	18 24 50.1	−11 58 22	1996 Sep	4.0	4	4.9	CH II	0.12	14
G20.08−0.13...................	18 25 22.6	−11 30 45	1998 Jul	3.4	7	5.4	UCH II	0.05	14
G23.95+0.16...................	18 31 40.8	−16 16 34	1998 Jul	5.8	9	4.0	H II	0.32	14
G24.49−0.04...................	18 33 22.8	−07 33 54	1997 Apr	3.5	1	5.5	. . .	. . .	. . .
W42	18 33 30.3	−07 14 42	1997 Apr	9.1	13	3.8	UCH II	. . .	
G28.86+0.07...................	18 41 07.9	−03 38 41	1998 Jul	8.5	5	4.2	. . .	. . .	. . .
W43S	18 43 26.7	−02 42 40	1998 Jul	8.5	4, 14	4.4	CH II	0.28	14
G31.41+0.31...................	18 44 59.5	−01 16 07	1997 Apr	7.9	12	4.5	UCH II	0.05	14
W43 Main 3	18 45 11.2	−01 57 57	1998 Jul	6.8	4	4.4	. . .	. . .	. . .
G31.44−0.26...................	18 46 57.5	−01 32 33	1997 Apr	10.7	9	5.6	UCH II	0.04	19
G32.05+0.06...................	18 47 02.0	−00 49 19	1998 Jul	8.5	9	4.7	. . .	. . .	
G32.80+0.20A/B	18 47 57.3	−00 05 28	1998 Jul	15.6	13	9.6	CH II	0.09	19
W44	18 50 46.1	+01 11 11	1998 Jul	3.7	9	5.8	CH II	0.06	14
S76E	18 53 45.6	+07 49 16	1998 Jul	2.1	1	7.0	H II	. . .	
G35.58−0.03...................	18 53 51.4	+02 16 29	1996 Oct	3.5	13	6.0	UCH II	0.02	19
G35.20−0.74...................	18 55 40.8	+01 36 30	1998 Jul	3.3	9	6.1	H II	. . .	
W49N	19 07 49.8	+09 01 17	1996 Oct	14.0	4	9.7	UCH II	0.01	22
W49S	19 07 58.2	+09 00 03	1999 Jul	14.0	4	9.7	UCH II	. . .	
OH 43.80−0.13	19 09 31.2	+09 30 51	1998 Jul	2.7	13	6.8	UCH II	0.01	19
G45.07+0.13...................	19 11 00.3	+10 45 42	1996 Sep	9.7	13	7.1	UCH II	0.04	14
G48.61+0.02...................	19 18 13.1	+13 49 44	1998 Jul	11.8	1	8.9	CH II	0.07	19
W51W	19 20 53.3	+14 20 47	1999 Jul	7.0	17	6.6	H II	. . .	
W51M	19 21 26.2	+14 24 36	1996 Oct	7.0	17	6.6	CH II	0.21	23
G59.78+0.06...................	19 41 04.2	+23 36 42	1998 Jul	2.2	1	7.6	UCH II	. . .	. . .
S87................................	19 44 14.0	+24 28 10	1996 Sep	1.9	15	7.6	UCH II	0.01	19
S88B	19 44 42.0	+25 05 30	1996 Jul	2.1	2	7.7	UCH II	0.01	14
K3-50.............................	19 59 50.1	+33 24 17	1997 Jun	9.0	4	10.1	CH II	0.18	19
ON 1	20 08 09.9	+31 22 42	1998 Jul	6.0	1	8.5	UCH II	0.02	19
ON 2S	20 19 48.9	+37 15 52	1998 Jul	5.5	1	8.9	H II	. . .	
ON 2N	20 19 51.8	+37 17 01	1998 Jul	5.5	1	8.9	CH II	0.07	14
S106	20 25 32.8	+37 12 54	1998 Jul	4.1	16	8.5	UCH II	0.01	19
W75N	20 36 50.5	+42 27 01	1998 Jul	3.0	4	8.6	UCH II	. . .	
DR 21S	20 37 13.8	+42 08 52	1999 Jul	3.0	4	8.6	UCH II	0.04	19
W75 (OH)	20 37 14.1	+42 12 12	1999 Jul	3.0	4	8.6	. . .	. . .	
G97.53+3.19...................	21 30 37.0	+55 40 36	1998 Jul	7.9	1	12.3	H II	. . .	
BFS 11−B........................	21 41 57.6	+65 53 17	1997 Dec	2.0	5	9.2	. . .	. . .	. . .
Cep A.............................	22 54 19.2	+61 45 44	1999 Jul	0.73	17	8.8	UCH II	. . .	. . .
NGC 7538.......................	23 11 36.1	+61 10 30	1997 Dec	2.8	2	9.9	UCH II	<0.01	24
S157..............................	23 13 53.1	+59 45 18	1997 Dec	2.5	2	9.7	CH II	0.10	19

NOTE.—Units of right ascension are hours, minutes, and seconds, and units of declination are degrees, arcminutes, and arcseconds.

REFERENCES.—(1) R_N, Paper I; (2) Blitz et al. 1982; (3) Harris & Wynn-Williams 1976; (4) Genzel & Downes 1977; (5) Braz & Epchtein 1983; (6) Chini et al. 1986; (7) Hofner et al. 1996; (8) Val'tts et al. 2000; (9) Solomon et al. 1987; (10) Zinchenko et al. 1994; (11) Hunter et al. 2000; (12) Churchwell et al. 1990; (13) Downes et al. 1980; (14) Wood & Churchwell 1989a; (15) Brand & Blitz 1993; (16) Wink et al. 1982; (17) Zhou et al. 1996; (18) Wilner et al. 1995; (19) Kurtz et al. 1994; (20) Hatchell et al. 2000; (21) Jaffe et al. 1984; (22) Dreher et al. 1984; (23) Scott 1978; (24) Turner & Matthews 1984.

in common (Olmi & Cesaroni 1999); and three sources in common (Beuther et al. 2002). Thirty-two of our sources were included in the CS $J = 1 \rightarrow 0$ and NH_3 survey of Anglada et al. (1996), while six sources were included in the $N_2H^+ J = 1 \rightarrow 0$ survey of Pirogov et al. (2003); however, we trace a denser gas component with the $J = 5 \rightarrow 4$ transition of CS.

2.2. *Observational Method*

The 230 GHz sidecab receiver with a 50 MHz AOS back-end was used for all observations (Kooi et al. 1992, 1998). The average velocity resolution was 0.119 km s^{-1}. The observing parameters and conditions are listed in Table 2. The standard chopper calibration method was used to measure T_A^* (Penzias & Burrus 1973). The beam size (θ_{mb}) at 244 GHz was 24″5 for the 1996 September through 1998 July observations. The secondary edge taper was increased from -5.2 to -8.5 dB in 1998 August (R. Chamberlin 2001, private communication; see Kooi 1998) resulting in a larger beam of 30″5 at 244 GHz (see Table 2). Only five sources were mapped using the larger beam size (W49S, W51W, DR 21S, W75 (OH), and Cep A).

Observations toward the peak of the CS $J = 5 \rightarrow 4$ integrated intensity were made in $C^{34}S$ $J = 5 \rightarrow 4$ and ^{13}CS $J = 5 \rightarrow 4$. All of the observations were made after the secondary edge taper was increased. The beam size at 241 GHz and 231 GHz was 31″0 and 32″5, respectively.

Determinations of the main beam efficiency, η_{mb}, were made on planets during each observing run. The average η_{mb} increased by 20% after the secondary edge taper was increased, excluding the last two observing sessions (01/02 and 06/02), where mirror alignment problems decreased the main beam efficiency. Average system temperatures ranged from 191 to 590 K during the observations. Pointing was checked every hour using planets. The average standard deviations in azimuth and zenith angle pointing were 5″ and 4″, respectively, for all of the observations, resulting in a 6″ pointing uncertainty. These errors, adding to about one-quarter beam, are upper limits to the actual pointing errors because they were mostly slow drifts over the time of a run and pointing was corrected by repeated measurements during each night.

The cores were mapped using the on-the-fly (OTF) mapping technique (e.g., Mangum et al. 2000) with an over-sampled 10″ grid in R.A.-decl. coordinates. The scan rate was set at 2″ s^{-1} to provide 5 s of integration time per spectrum. On some occasions, the maps were repeated for higher signal-to-noise ratios. The map was extended until the CS $J = 5 \rightarrow 4$ line was not detected or negligible compared with the peak. The average rms per spectrum in the maps varied between 0.1 and 0.6 K.

3. RESULTS

The integrated intensity of the CS $J = 5 \rightarrow 4$ transition was calculated using

$$I(T_A^*) = \int_{v_1}^{v_2} T_A^* \, dv \,, \tag{1}$$

$$\sigma_{I(T_A^*)}^2 = \langle \sqrt{\Delta v_{line} \delta v_{chan}} \sigma_{T_A^*} \rangle_{map}^2 + \left(\frac{\Delta v_{line}}{\Delta v_{lft} + \Delta v_{rt}} \right)^2 \sigma_{I_{base}}^2 \,, \tag{2}$$

where $\Delta v_{line} = v_2 - v_1$ is a velocity interval that includes the entire line (as distinct from the FWHM of the line), Δv_{lft} and Δv_{rt} are the velocity intervals of the left and right baselines, δv_{chan} is the spectrometer velocity resolution, and $\sigma_{I_{base}}$ is the standard deviation of the integrated intensity of the total baseline ($\Delta v_{lft} + \Delta v_{rt}$) calculated over all of the spectra in the map. The first term in the integrated intensity error is the theoretical error and assumes no deviation from a linear baseline. The second term in the integrated intensity error compensates for residual variations in the baseline after a linear baseline was removed. This average error in the integrated intensity is added in quadrature to the average of the theoretical error for the integrated intensity, calculated for each spectrum in the map. The theoretical error (first term) typically dominates. The integrated intensity is placed on the T_R^* scale (Kutner & Ulich 1981) by dividing equation (1) by the η_{mb} appropriate for the night the object was observed (Table 2). This calibration procedure is described in § 2 of Paper II. An assumed error in η_{mb} (10%) was propagated into the uncertainty in $I(T_R^*)$.

Contour maps of integrated intensity are shown in Figures 2–12. The average extent of the maps is ±50″, but larger

TABLE 2
CSO OBSERVATIONS 1996–2002

| UT Date	Transition	ν (GHz)	θ_{mb} (arcsec)	η_{mb}	Pointing (σ_{AZ}, σ_{ZA}) (arcsec)
1996 Sep	CS $J = 5 \rightarrow 4$	244.9355680	24.5	0.56	(3.8, 2.7)
1996 Oct	CS $J = 5 \rightarrow 4$	244.9355680	24.5	0.56	(3.8, 2.7)
1996 Dec	CS $J = 5 \rightarrow 4$	244.9355680	24.5	0.54	(1.9, 3.2)
1997 Apr	CS $J = 5 \rightarrow 4$	244.9355680	24.5	0.56	(6.6, 3.2)
1997 Jun	CS $J = 5 \rightarrow 4$	244.9355680	24.5	0.58	(2.0, 5.2)
1997 Dec	CS $J = 5 \rightarrow 4$	244.9355680	24.5	0.55	(4.4, 5.2)
1998 Jul	CS $J = 5 \rightarrow 4$	244.9355680	24.5	0.57	(6.7, 2.7)
1998 Dec	$C^{34}S$ $J = 5 \rightarrow 4$	241.0161940	31.0	0.66	(2.4, 3.4)
	^{13}CS $J = 5 \rightarrow 4$	231.2209960	32.5	0.66	
1999 Jul	CS $J = 5 \rightarrow 4$	244.9355680	30.5	0.64	(5.6, 5.4)
2001 Jul	$C^{34}S$ $J = 5 \rightarrow 4$	241.0161940	31.0	0.73	(3.0, 3.4)
	^{13}CS $J = 5 \rightarrow 4$	231.2209960	32.5	0.73	
2002 Jan	$C^{34}S$ $J = 5 \rightarrow 4$	241.0161940	31.0	0.54	(12.7, 3.8)
2002 Jun	$C^{34}S$ $J = 5 \rightarrow 4$	241.0161940	31.0	0.61	(4.2, 4.8)
	^{13}CS $J = 5 \rightarrow 4$	231.2209960	32.5	0.59	
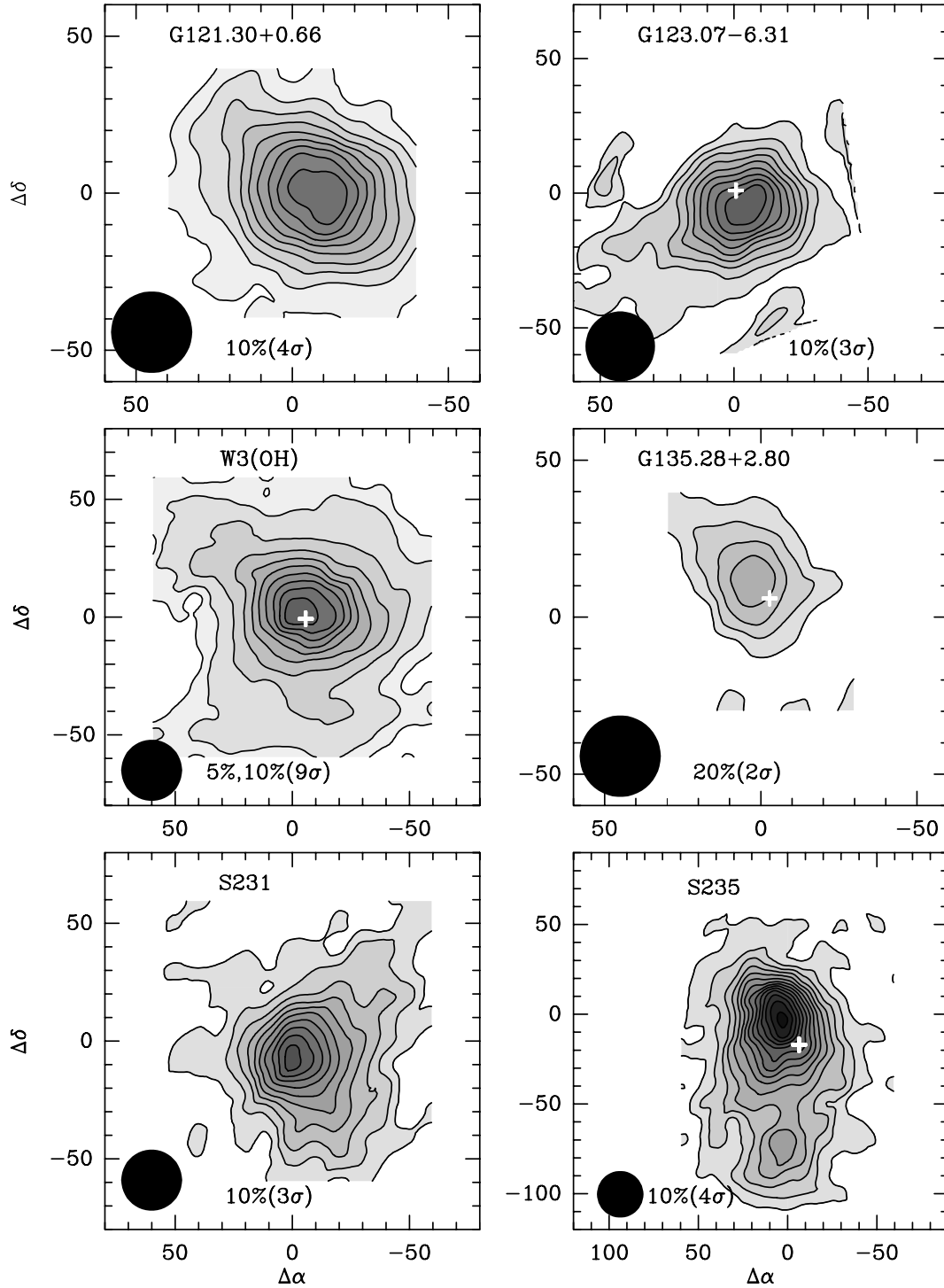
Fig. 2.—Contour maps of CS $J = 5 \rightarrow 4$ integrated intensity with the FWHM beam size shown in the lower left corner. The contour levels are indicated at the bottom of each panel. For instance, " 5%, 10% (5 σ) " means the first contour is 5% the peak intensity, the next contour is 10% the peak intensity, and the contour interval is 10% or 5 σ. The plus sign marks the location of the nearest H II region to the water maser position. The water maser is at (0, 0).

maps were made where necessary. The lowest contour is at least $2\sigma_I$, and typical contour intervals are 10% of the peak intensity. The cores were well detected with a median peak signal-to-noise ratio of 40 and peak integrated intensities that range from 5.5 to 208 K km s^{-1}. The median separation of the peak of CS integrated intensity from the 350 μm dust continuum peak (Mueller et al. 2002b) is 7$''$. The peak integrated intensity correlates well ($r = 0.85$) with the sub-

millimeter flux at 350 μm (Fig. 13); a fit to the logarithms indicates a relationship that is nearly linear: $\log I(T_R^*) = (-0.60 \pm 0.01) + (0.92 \pm 0.05) \log S_{350 \, \mu m}$. Objects that are bright at 350 μm are also strong emitters in the CS $J = 5 \rightarrow 4$ line and the dust continuum and CS emission are coincident. Since the 350 μm dust continuum is optically thin, it is a good tracer of mass along each line of sight. The strong correlation between $I(T_R^*)$ and $S_{350 \, \mu m}$ confirms
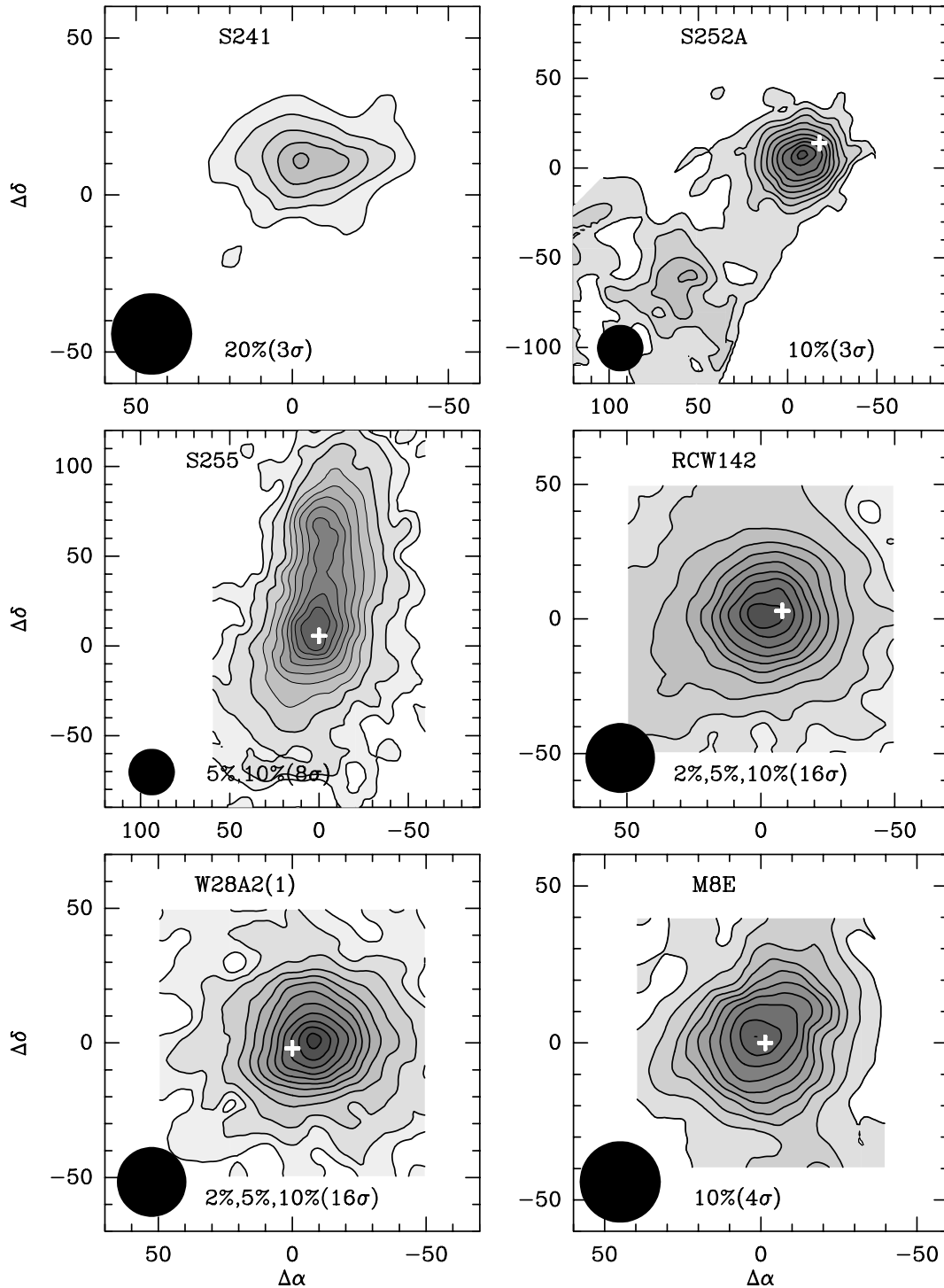
Fig. 3.—Contour maps of CS $J = 5 \rightarrow 4$ integrated intensity with the FWHM beam size shown in the lower left corner. The contour levels are indicated at the bottom of each panel. For instance, "5%, 10% (5 σ)" means the first contour is 5% the peak intensity, the next contour is 10% the peak intensity, and the contour interval is 10% or 5 σ. The plus sign marks the location of the nearest H ii region to the water maser position. The water maser is at (0, 0).

that high-J lines of CS are excellent tracers of dense, warm gas.

An extensive literature search using the SIMBAD database was performed to find H ii regions associated with the dense CS cores. Only 12 cores (19%) were found with no obvious, direct association with radio continuum emission (e.g., UCH ii). When possible, the 2 cm size is reported in Table 1. Using the taxonomy of Kurtz (2002), H ii regions

are classified as ultracompact (UCH ii) if the diameter is ≤0.1 pc, compact (CH ii) if the diameter is ≤0.5 pc, and an extended H ii region if the diameter is greater than 0.5 pc or clearly associated with a classical H ii region. The classifications of several UCH ii are unclear since no 2 cm sizes are reported in the literature. Some of the cores contain multiple UCH ii regions (see Conti & Blum 2002, W49N region), but only the nearest H ii region to the water maser peak is
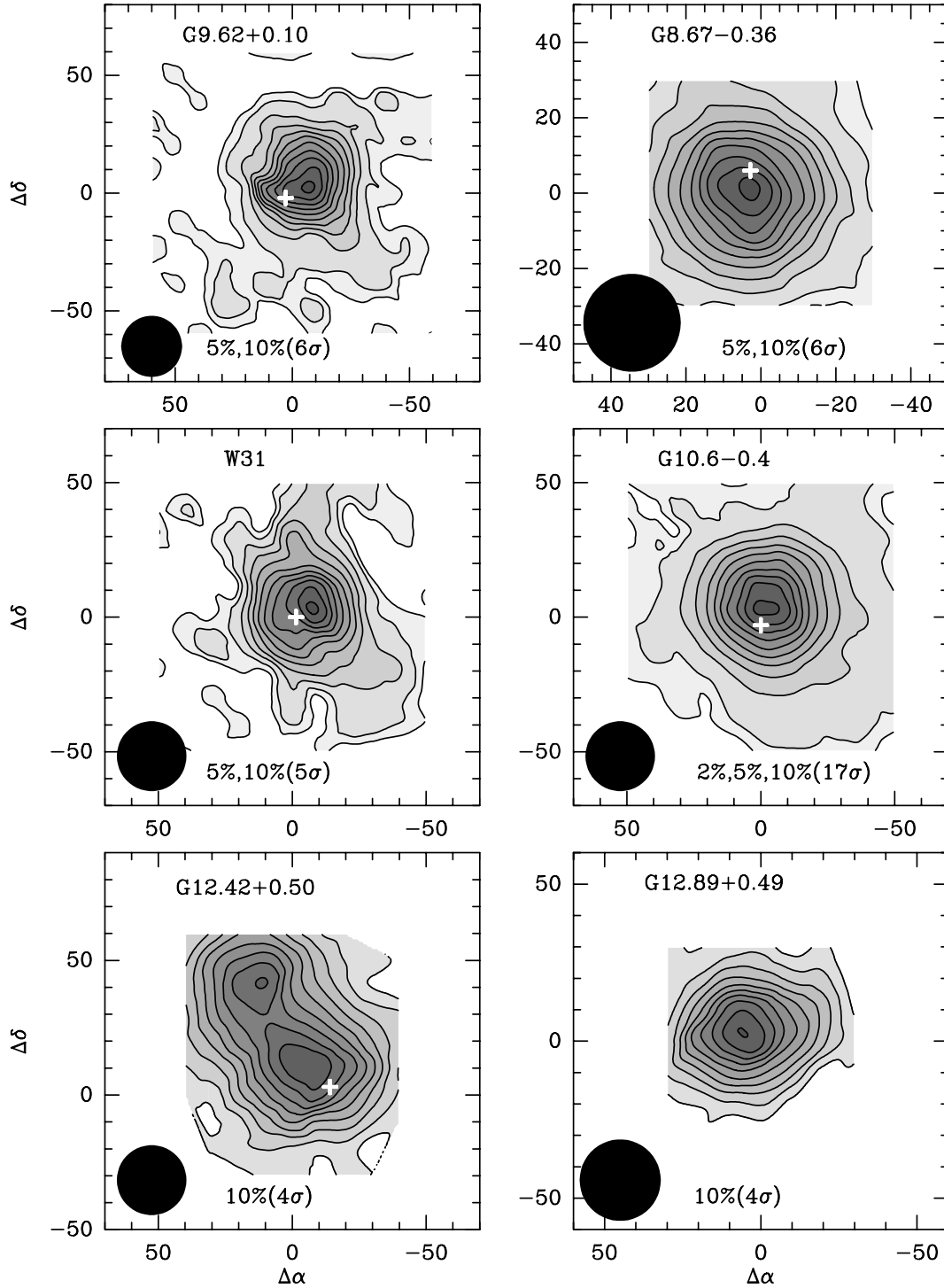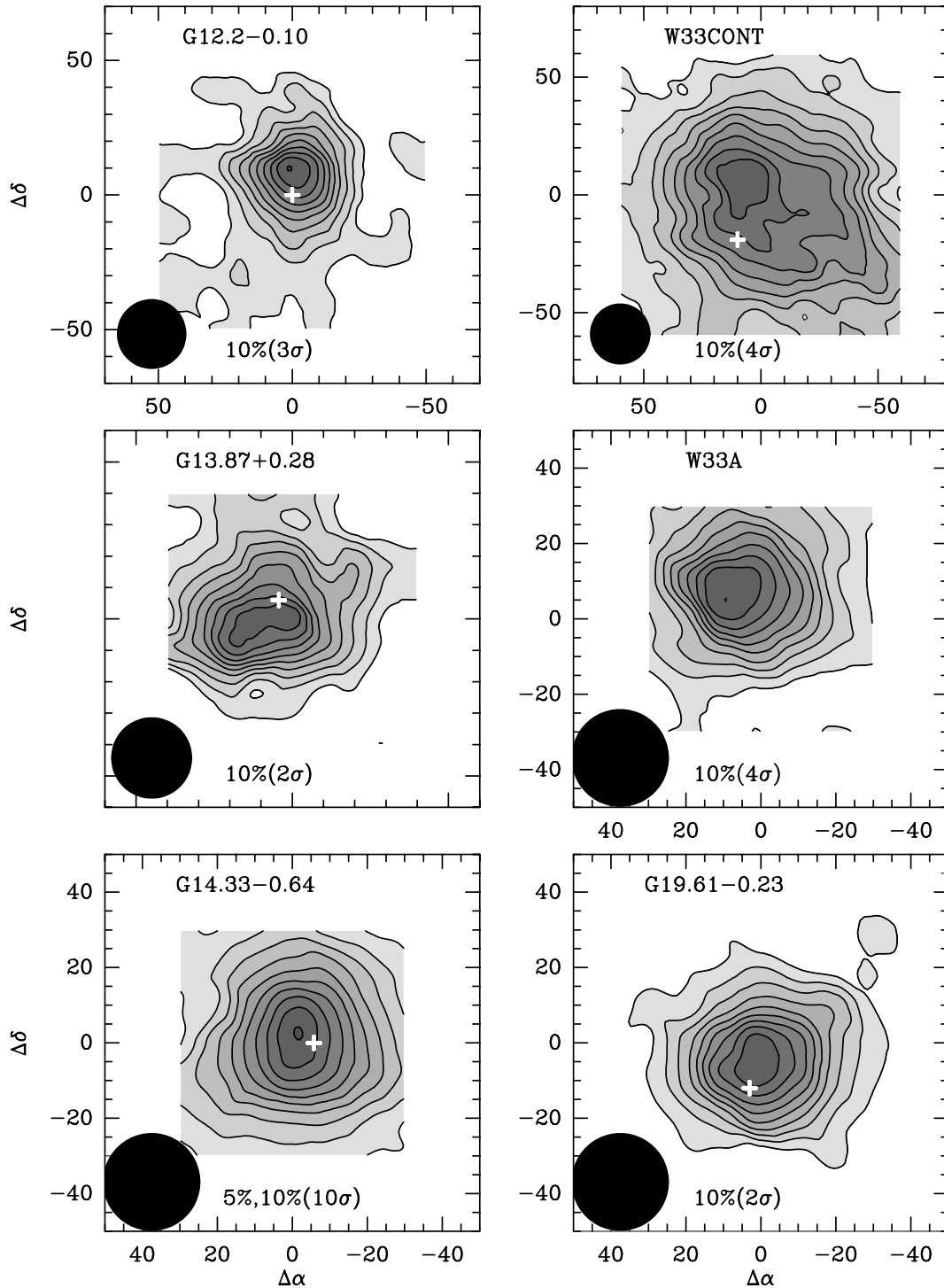
FIG. 4.—Contour maps of CS $J = 5 \rightarrow 4$ integrated intensity with the FWHM beam size shown in the lower left corner. The contour levels are indicated at the bottom of each panel. For instance, " 5%, 10% (5 σ) " means the first contour is 5% the peak intensity, the next contour is 10% the peak intensity, and the contour interval is 10% or 5 σ. The plus sign marks the location of the nearest H II region to the water maser position. The water maser is at (0, 0).

plotted to minimize obscuration of the CS map (Figs. 2–12). The CS integrated intensity is weaker for sources with no known radio continuum emission ($\langle I(T_R^*) \rangle = 25.9 \pm 23.1$ K km s^{-1}, $\mu_{1/2} = 19.7$ K km s^{-1}) than for sources with UCH II regions ($\langle I(T_R^*) \rangle = 50.4 \pm 41.0$ K km s^{-1}, $\mu_{1/2} = 35.7$ K km s^{-1}) and CH II or H II regions ($\langle I(T_R^*) \rangle = 54.6 \pm 58.0$ K km s^{-1}, $\mu_{1/2} = 32.0$ K km s^{-1}).

The CS centroid is generally close to the water maser peak with a median centroid distance of 8″; only eight cores (13%) have CS centroids more than $\theta_{mb}/2$ away from the water maser position. The median distance between the CS centroid and H II regions was 8″, less than one-third of the beam FWHM but larger than the average pointing uncertainty. The peak CS emission is directly associated with the

Fig. 5.—Contour maps of CS $J = 5 \rightarrow 4$ integrated intensity with the FWHM beam size shown in the lower left corner. The contour levels are indicated at the bottom of each panel. For instance, "5%, 10% (5 σ)" means the first contour is 5% the peak intensity, the next contour is 10% the peak intensity, and the contour interval is 10% or 5 σ. The plus sign marks the location of the nearest H II region to the water maser position. The water maser is at (0, 0).

H II region in 36 (57%) of those cores, while 15 H II regions are more than $\theta_{mb}/2$ away from the CS peak. The dense gas traced by CS $J = 5 \rightarrow 4$ emission is clearly associated with water maser emission and often associated with an (UC, C-)H II region.

The majority of cores (46) are isolated within the regions mapped (1'.7 field of view for the average map size). Seventeen cores (27%) have companions with a median separation

of 0.93 pc. Three cores have more than two distinct companions within the mapped region (S87, W51W, W75 (OH)).

Spectra toward the W49N region (also denoted W49A North) display two blended velocity components. The CS $J = 5 \rightarrow 4$ lines clearly show a peak near 4 and 12 km s^{-1} in all spectra in the map. There is considerable debate in the literature over the correct interpretation of the two velocity components: are there multiple clouds (see Serabyn,
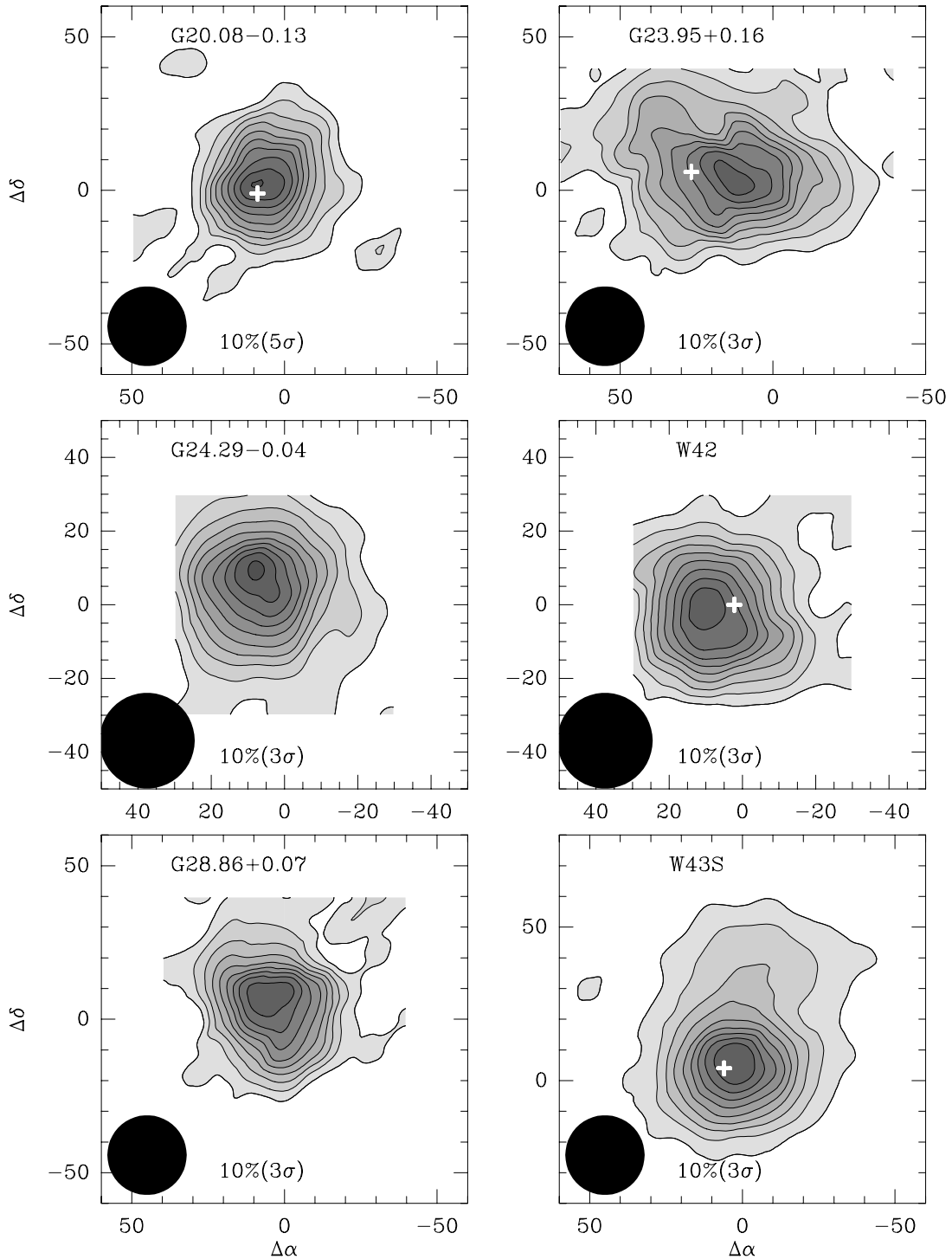
FIG. 6.—Contour maps of CS $J = 5 \rightarrow 4$ integrated intensity with the FWHM beam size shown in the lower left corner. The contour levels are indicated at the bottom of each panel. For instance, " 5%, 10% (5 σ) " means the first contour is 5% the peak intensity, the next contour is 10% the peak intensity, and the contour interval is 10% or 5 σ. The plus sign marks the location of the nearest H II region to the water maser position. The water maser is at (0, 0).

Güsten, & Schulz 1993) or is this purely an optical depth effect (see Dickel et al. 1999)? Since the two components are also observed in the C^{34}S and ^{13}CS isotopomers, we shall analyze W49N as two separate clouds with the caveat that this region is very complicated. The integrated intensity for two-component Gaussian fits to the spectra are shown in Figure 8.

The integrated intensities for C^{34}S $J = 5 \rightarrow 4$ and ^{13}CS $J = 5 \rightarrow 4$ observations are listed in Table 3. Forty-nine cores were detected in the C^{34}S $J = 5 \rightarrow 4$ transition, while seven cores were not detected to an average 3 σ T_A^* level of 300 mK (G135.28+2.80, S241, S252A, G24.49−0.04, S106, BFS 11−B, S157). The average integrated intensity is $\langle I(T_R^*) \rangle = 6.5 \pm 7.5$ K km s^{-1} with a median of 4.0 K km
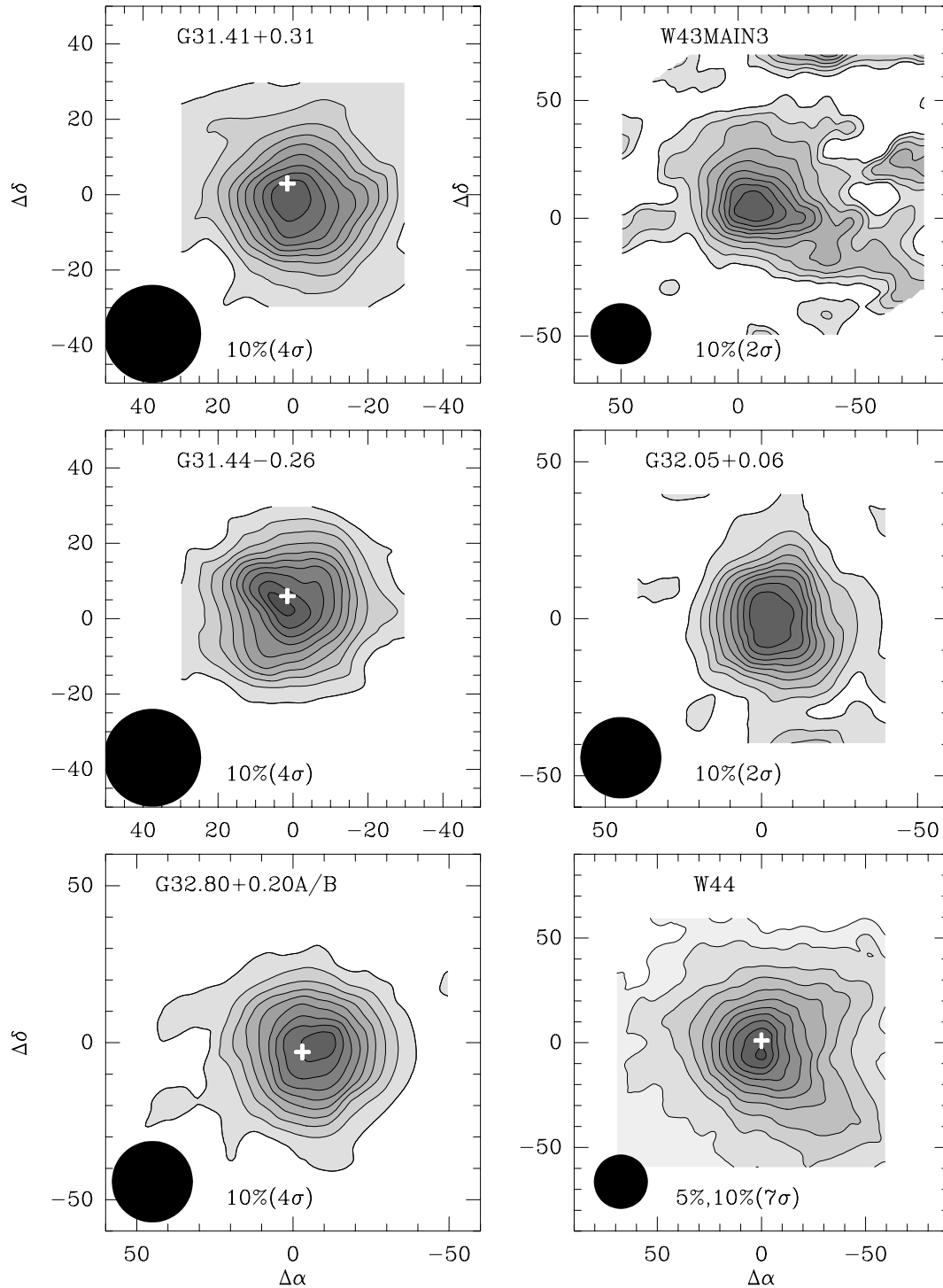
Fig. 7.—Contour maps of CS $J = 5 \rightarrow 4$ integrated intensity with the FWHM beam size shown in the lower left corner. The contour levels are indicated at the bottom of each panel. For instance, "5%, 10% (5 σ)" means the first contour is 5% the peak intensity, the next contour is 10% the peak intensity, and the contour interval is 10% or 5 σ. The plus sign marks the location of the nearest H II region to the water maser position. The water maser is at (0, 0).

s^{-1}, both values a factor of 10 lower than the corresponding values for CS $J = 5 \rightarrow 4$. Nine of the strongest cores were also observed in ^{13}CS $J = 5 \rightarrow 4$ with all of the cores detected. The average ratio between the integrated intensity of C^{34}S $J = 5 \rightarrow 4$ and ^{13}CS $J = 5 \rightarrow 4$ is 2.6, consistent with the observed interstellar isotope ratio between ^{34}S and ^{13}C (Wilson & Rood 1994).

4. ANALYSIS

4.1. *Core Size and Aspect Ratio*

Previous studies (e.g., van der Tak et al. 2000; Hatchell et al. 2000; Beuther et al. 2002) and our modeling of the dust continuum emission (Mueller et al. 2002b) indicate that the distribution of density is well fitted by a power
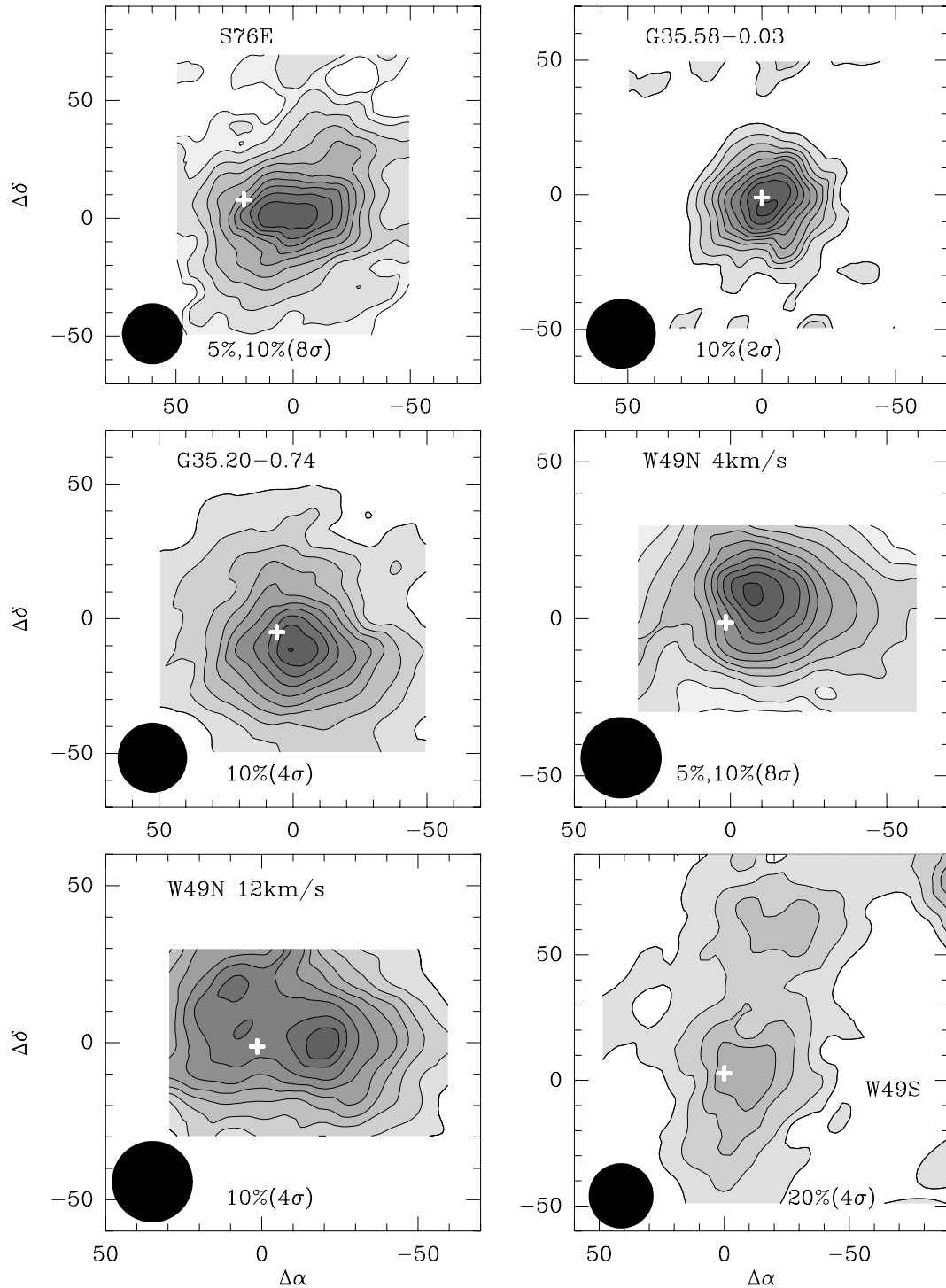
Fig. 8.—Contour maps of CS $J = 5 \rightarrow 4$ integrated intensity with the FWHM beam size shown in the lower left corner. The contour levels are indicated at the bottom of each panel. For instance, " 5%, 10% (5 σ) " means the first contour is 5% the peak intensity, the next contour is 10% the peak intensity, and the contour interval is 10% or 5 σ. The plus sign marks the location of the nearest H II region to the water maser position. The water maser is at (0, 0).

law, $n(r) \propto r^{-p}$. Since power laws have no intrinsic size scale, assigning a size to such distributions can be highly misleading. Following long tradition, we will calculate a nominal radius for each source from a Gaussian deconvolution of the beam, and we will use this radius for calculation of masses. We caution that this radius should be viewed strictly as a fiducial radius, with no physical signif-

icance. We discuss later the likely corrections to masses, etc., that result from continuation of power laws to larger scales.

The angular extent of each map at the half power level was determined by finding the area within the contour at half I_{peak}, $A_{1/2}$, and calculating the angular radius of a circle with the same area. The nominal core radius, R_{CS}, was
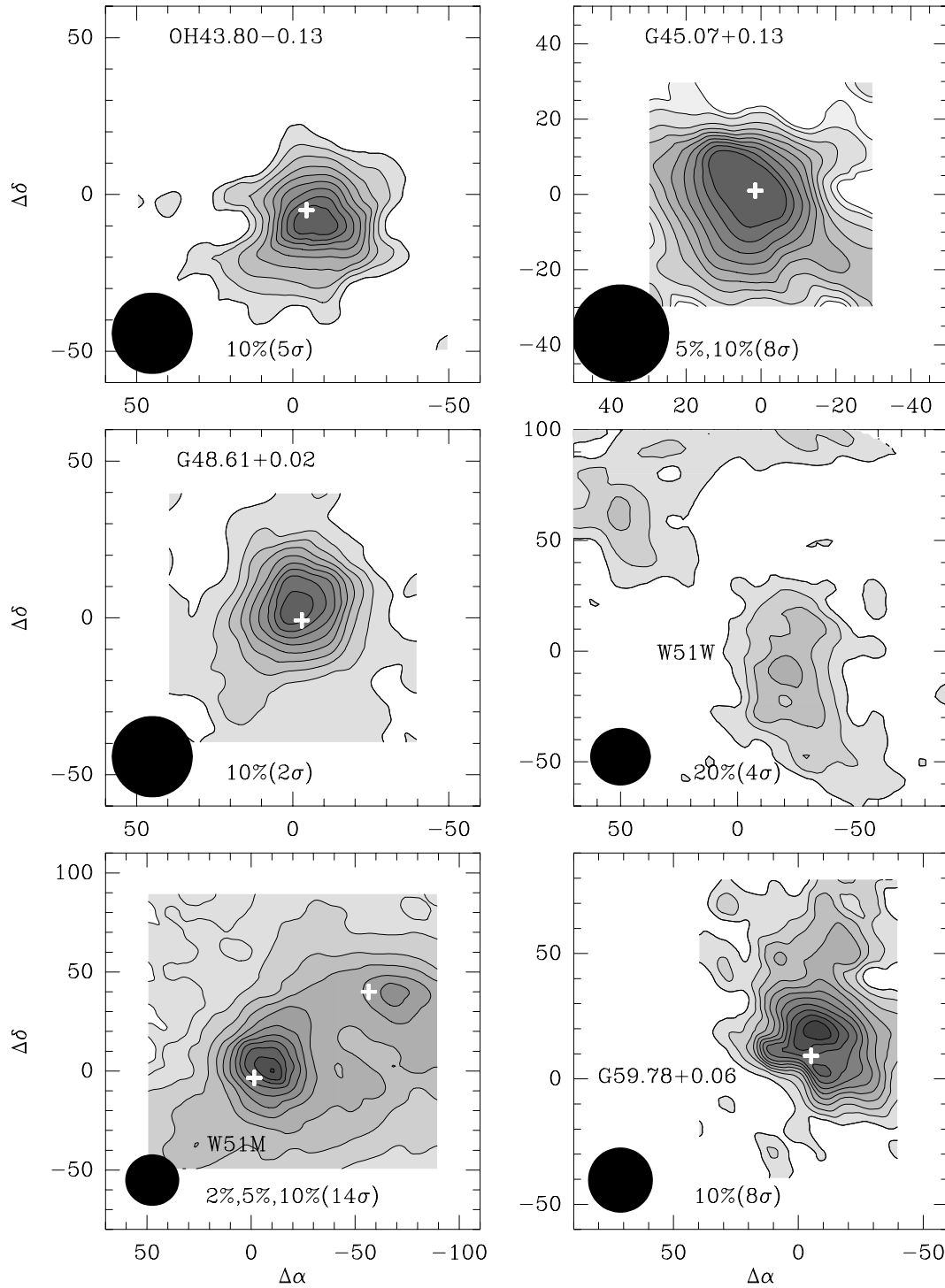
Fig. 9.—Contour maps of CS $J = 5 \rightarrow 4$ integrated intensity with the FWHM beam size shown in the lower left corner. The contour levels are indicated at the bottom of each panel. For instance, "5%, 10% (5 σ)" means the first contour is 5% the peak intensity, the next contour is 10% the peak intensity, and the contour interval is 10% or 5 σ. The plus sign marks the location of the nearest H II region to the water maser position. The water maser is at (0, 0).

determined by deconvolving the telescope beam (θ_{mb}) assuming both are Gaussians:

$$R_{\mathrm{CS}} = D\left(\frac{A_{1/2}}{\pi} - \frac{\theta_{\mathrm{mb}}^2}{4}\right)^{1/2}, \qquad (3)$$

where D is the distance to the core. Similarly, the decon-

volved angular size, θ_{dec}, is found from

$$\theta_{\mathrm{dec}} = \left(\frac{4A_{1/2}}{\pi} - \theta_{\mathrm{mb}}^2\right)^{1/2}. \qquad (4)$$

The core radius and uncertainty are listed in Table 4. The quoted uncertainty in core radius is derived from the
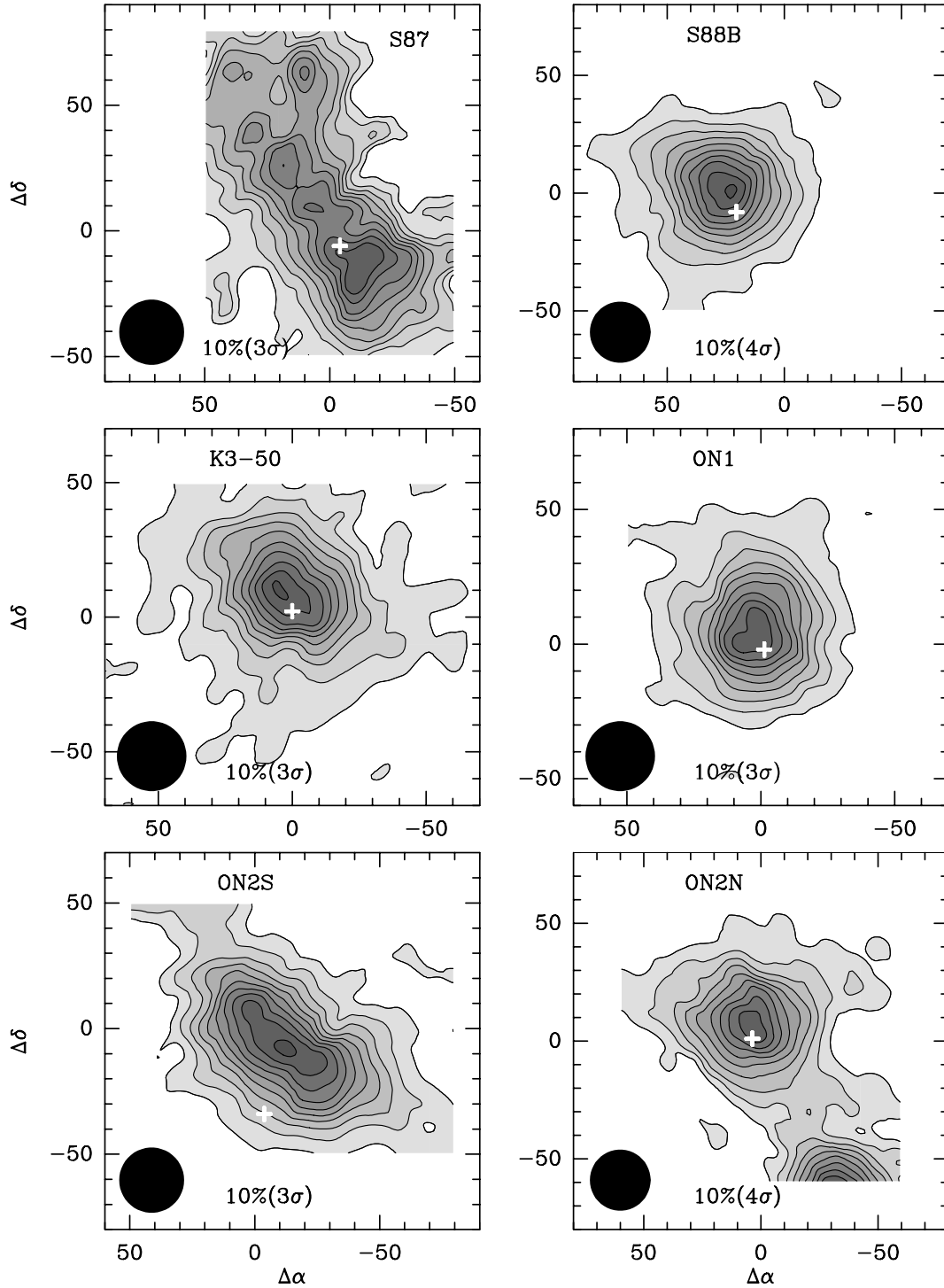
FIG. 10.—Contour maps of CS $J = 5 \rightarrow 4$ integrated intensity with the FWHM beam size shown in the lower left corner. The contour levels are indicated at the bottom of each panel. For instance, " 5%, 10% (5 σ) " means the first contour is 5% the peak intensity, the next contour is 10% the peak intensity, and the contour interval is 10% or 5 σ. The plus sign marks the location of the nearest H II region to the water maser position. The water maser is at $(0, 0)$.

uncertainty in area of the core ($A_{1/2}$) and the uncertainty in the main beam FWHM, assumed to be 10% of θ_{mb}. The distance uncertainty actually dominates the uncertainty in R_{CS}, but it is ignored in this analysis since σ_D is difficult to determine. Since the distance may be uncertain by at least 50%, the core radius would be uncertain by the same factor.

Almost all (57) of the cores have clearly defined values for R_{CS}. The remainder (six cores) have multiple peaks too close

together to allow unambiguous determination of a FWHM angular size (see Table 4). This sample of 57 cores provides the sample for the statistical analysis in the rest of the paper. The majority of cores (36, 63%) have *deconvolved* sizes that are larger than the main beam FWHM, indicating that they are well resolved (Fig. 14). The dashed line in Figure 14 indicates the R_{CS} at each distance for which the deconvolved source size equals the FWHM beam size. The largest core
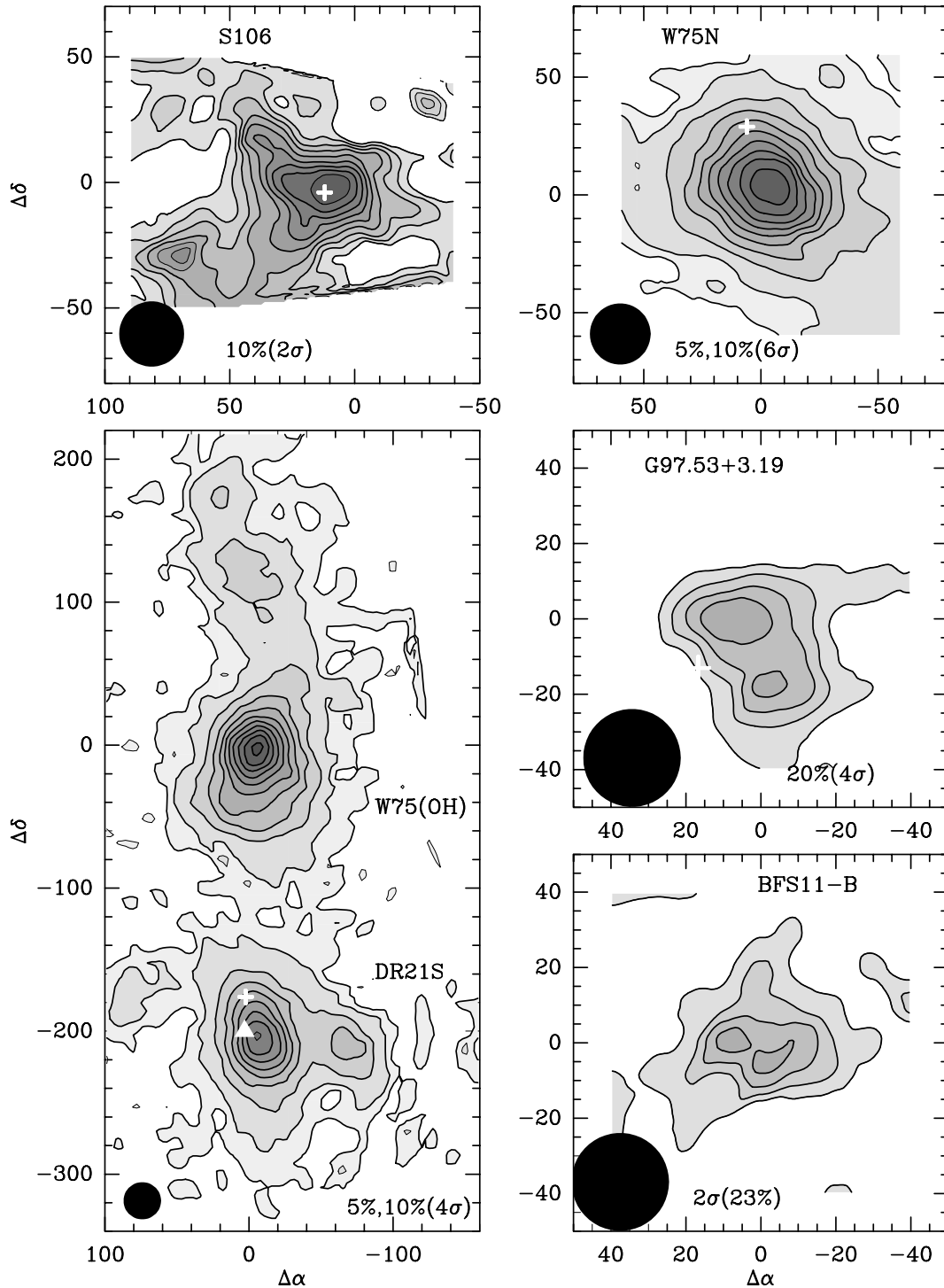
Fig. 11.—Contour maps of CS $J = 5 \rightarrow 4$ integrated intensity with the FWHM beam size shown in the lower left corner. The contour levels are indicated at the bottom of each panel. For instance, " 5%, 10% (5 σ) " means the first contour is 5% the peak intensity, the next contour is 10% the peak intensity, and the contour interval is 10% or 5 σ. The plus sign marks the location of the nearest H II region to the water maser position. The water maser is at (0, 0) except in the W75 (OH)/DR 21S map where a second water maser is marked by a triangle near the peak of DR 21S.

was W49S with $R_{CS} = 1.53$ pc, while the smallest cores were S252A and G121.30+0.66, with $R_{CS} = 0.10$ pc.

The average over the sample is $R_{CS} = 0.37 \pm 0.26$ pc, while the median core size is 0.32 pc. The distribution of $\log R_{CS}$ is peaked for core sizes near the mean and median values (Fig. 15a). For a source at the median distance of the sample, 4.0 kpc, $R_{CS} < 0.19$ pc would fail our criterion

($\theta_{dec} \geq \theta_{mb}$) for being well resolved. The median distance bias is shown as a horizontal dotted line in Figure 14. The average over the sample is smaller than the average core radius of 0.5 ± 0.4 pc determined in Paper II for the 25 cores with cross-scans. Sources not directly associated with radio continuum emission ($N = 12$) are slightly smaller than cores with radio continuum emission ($R_{CS} = 0.28 \pm 0.14$ pc and
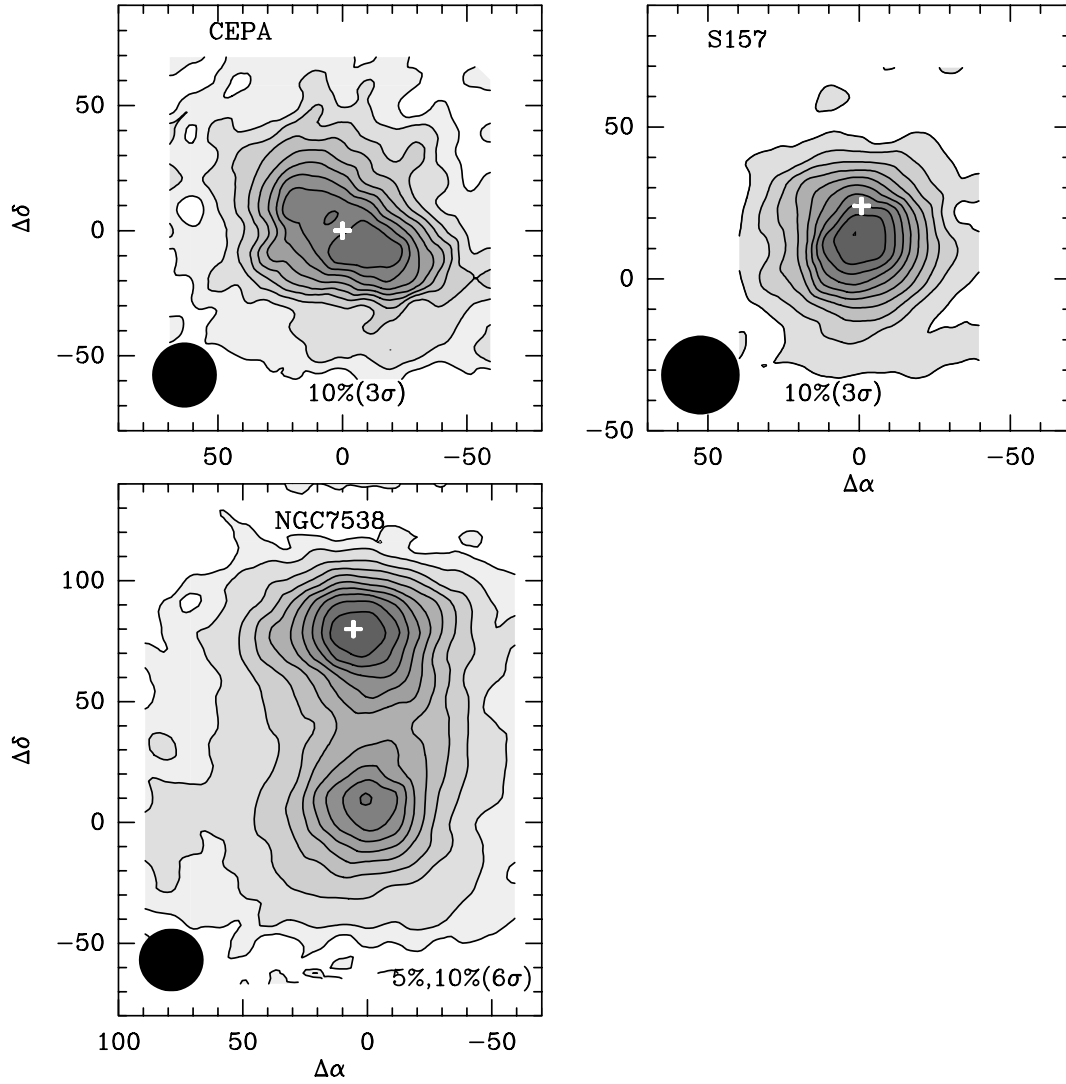
FIG. 12.—Contour maps of CS $J = 5 \rightarrow 4$ integrated intensity with the FWHM beam size shown in the lower left corner. The contour levels are indicated at the bottom of each panel. For instance, " 5%, 10% (5 σ) " means the first contour is 5% the peak intensity, the next contour is 10% the peak intensity, and the contour interval is 10% or 5 σ. The plus sign marks the location of the nearest H II region to the water maser position. The water maser is at (0, 0).

$\mu_{1/2} = 0.25$ pc; see Fig. 15a). There is no statistically significant difference between the sizes of cores associated with UCH II, CH II, or H II regions and the complete sample.

The process of finding a FWHM size might vary with the intensity of the core, introducing a bias into the size distribution. The integrated intensity is plotted against R_{CS} in Figure 14 for 57 cores. There is no observed correlation ($r = 0.07$) between CS intensity and core radius over a wide range in both variables.

The 350 μm dust continuum from 24 sources from our survey was modeled with a radiative transfer code by Mueller et al. (2002b). The best-fit power-law index, $p = -\log n / \log r$, is listed in Table 5. Convolving a power-law intensity distribution with a Gaussian beam pattern should result in deconvolved core sizes that are somewhat larger than θ_{mb} (e.g., Terebey, Chandler, & André 1993). Flatter power laws produce larger deconvolved source sizes than steeper power laws. This correlation was observed toward a sample of low-mass cores observed at 850 μm with SCUBA (Shirley, Evans, & Rawlings 2000; Young et al. 2003). A weak correlation ($r = -0.55$) is observed between

the best-fit power-law index and the deconvolved source size determined from our CS maps (Fig. 16). This correlation is likely real since the observations were made with two different instruments, SHARC (Hunter, Benford, & Serabyn 1996) and the CSO 230 GHz receiver, with different beam sizes (14″ and 24″.5, respectively). For power-law density distributions, the deconvolved source size may be used as a rough guess of p if the correlation is calibrated.

An alternative method for determining the core radius is to measure the sizes of the cores at the same intensity level. For instance, the core radius, R_{10}, at an intensity level of $I(T_R^*) = 10$ K km s^{-1} is calculated (Table 4) using the same method as for R_{CS} and deconvolving a Gaussian telescope beam:

$$R_{10} = D \left[\frac{A_{10}}{\pi} - \frac{\theta_{mb}^2 \ln(I_{peak}(T_R^*)/10)}{4 \ln 2} \right]^{1/2} . \quad (5)$$

R_{10} was unresolved for 11 cores ($R_{10} < R_{CS}$), was too large to be determined for six cores ($R_{10} >$ extent of the map), and encompassed more than one core in four cases. The
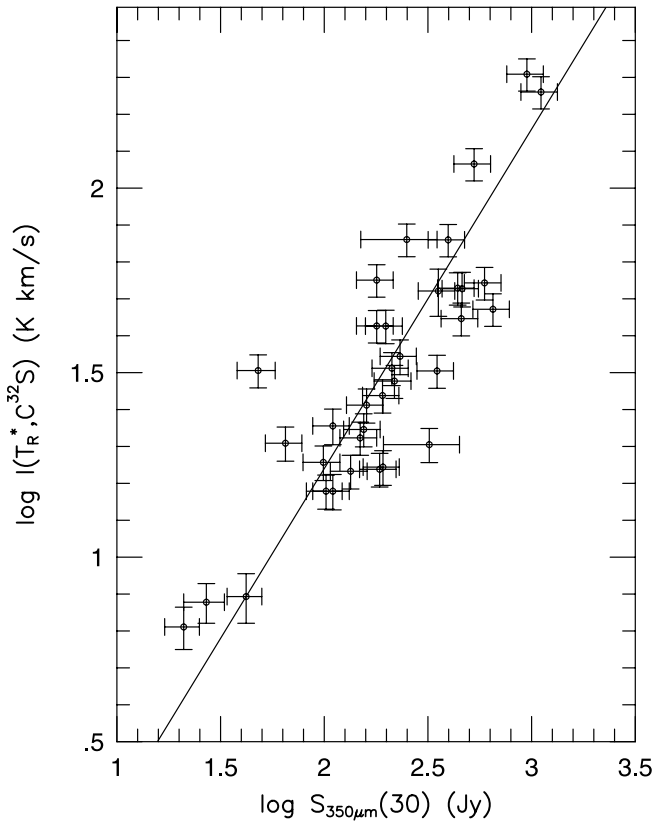
FIG. 13.—Logarithm of the peak CS 5–4 integrated intensity vs. the logarithm of the 350 μm flux density in a 30″ aperture (Mueller et al. 2002b). The solid line indicates the best-fit relation: $\log I(T_R^*) = (-0.60 \pm 0.01) + (0.92 \pm 0.05) \log S_{350\ \mu m}$.

average core size for 33 cores was 0.50 ± 0.32 pc with a median size of 0.43, 35% larger than for R_{CS}. Since the choice of the intensity level is arbitrary and R_{CS} can be defined for many more cores, R_{CS} is the core radius used in most comparisons and calculations in this paper. R_{10} is used in § 4.2 for an alternative calculation of the line width–size relationship to explore the sensitivity of the results to this definition.

Aspect ratios for each core were determined from the ratio of major to minor axis for the 20% peak contour (Table 4). The 20% peak contour is well detected and resolved for the entire sample ($\langle\sigma_{20\%}\rangle = 10\sigma_I$). The distribution of aspect ratios (Fig. 15b) is strongly peaked toward low ($(a/b)_{obs} < 1.4$) aspect ratios, indicating that the observed contours are consistent with circular symmetry. The mean aspect ratio is 1.26 ± 0.22, while the largest observed aspect ratio is 1.8 (ON 2S). The cores are observed in projection, making $(a/b)_{obs}$ a lower limit to the actual aspect ratio. The position angle of the major axis, measured counterclockwise from north, is listed in Table 4. The histogram of position angles for cores with $(a/b)_{obs} \geq 1.2$ is plotted in Figure 15c. There is no bias in the core elongation observed along the scan direction of the OTF map (90°), indicating that the aspect ratios are unaffected by any beam smearing from the OTF method.

Young et al. (2003) report a correlation between $(a/b)_{obs}$ and p toward low-mass cores; flatter power laws ($p \sim 1$) are associated with more elongated cores. Using the p-values from Mueller et al. (2002b) and the CS aspect ratios, we find

no evidence for a correlation in this sample (Fig. 16). It is necessary to use the CS data to determine the aspect ratio since Mueller et al. were unable to determine reliable aspect ratios because of the effects of chopping.

4.2. Line Width–Size Relationship

The FWHM line width, $\Delta v(C^{32}S)$, for each core was determined from a Gaussian fit to a spectrum produced by convolving the data to an effective size corresponding to the half-power contour. The average line width for the sample of 63 cores was $\Delta v(C^{32}S) = 5.6 \pm 2.2$ km s^{-1}. A few cores show evidence for self-absorption and other optical depth effects. For a Gaussian line shape, the broadening due to optical depth can be expressed by

$$\frac{\Delta v}{\Delta v_o} = \frac{1}{\sqrt{\ln 2}} \sqrt{\ln\left\{\tau / \left[\ln\frac{2}{1+\exp(-\tau)}\right]\right\}} , \qquad (6)$$

where Δv_o is the optically thin line width (Phillips et al. 1979). We can use the C^{34}S $J = 5 \to 4$ line width to test optical depth effects. The CS to C^{34}S line width ratio for 49 cores was 1.3 ± 0.4 corresponding to an average optical depth of $\tau = 1.7$ (Fig. 17). Therefore, $\Delta v(C^{34}S)$ should be used when possible in calculations sensitive to the line width. We checked the optical depth of C^{34}S by observing ^{13}CS $J = 5 \to 4$ toward nine of the brightest cores. The C^{34}S line widths are consistent with being optically thin for all but three cores (Fig. 17).

The line width–size relationship for 51 cores using $\Delta v(C^{34}S)$ is plotted in Figure 18. The data were fitted with a least-squares method, including statistical errors in both quantities (Press et al. 1992) to give $\log \Delta v(C^{34}S) = (0.92 \pm 0.01) + (0.43 \pm 0.02) \log R_{CS}$. The linear correlation coefficient is low ($r = 0.36$). For comparison, a fit using robust estimation (Press et al. 1992), which is less sensitive to outliers, gives a shallower slope, $\log \Delta v(C^{34}S) = 0.77 + (0.17) \log R_{CS}$. If we average these two slopes, then $\Delta v(C^{34}S)$ is roughly proportional to $R_{CS}^{0.3}$. This slope of the line width–size relationship is consistent with the findings of Caselli & Myers (1995), who find a shallower line width–size relationship for "high-mass" regions ($\Delta v \propto R^{0.21 \pm 0.03}$) compared with "low-mass" ($<$few $M_\odot$) regions ($\Delta v \propto R^{0.53 \pm 0.07}$) probed by ^{13}CO and C^{18}O. Various studies using different tracers (NH$_3$, ^{12}CO, etc.) find line width–size relationships that vary between $\Delta v \sim R^{0.2}$ to $R^{0.8}$. (e.g., Brand & Wouterloot 1995; Jijina, Myers, & Adams 1999; and Brand et al. 2001). Alternatively, if we calculate the line width–size relationship using R_{10} instead of R_{CS} (Fig. 18, *bottom panel*), the least-squares fit ($r = 0.43$), $\log \Delta v(C^{34}S) = (0.87 \pm 0.01) + (0.65 \pm 0.03) \log R_{10}$, and robust estimation, $\log \Delta v(C^{34}S) = 0.78 + (0.20) \log R_{10}$, do not agree well. It is difficult to rigorously compare the results from our sample because the correlations are very weak and the distance uncertainty is large enough to eliminate the observed correlations.

The more important point is that the line widths are all much larger at a given radius than those found in either "low-mass" or "high-mass" regions by Caselli & Myers (1995). For the average core size in our sample, the average C^{34}S line width is 4 times larger than the "high-mass" prediction and 5 times larger than the "low-mass" prediction of Caselli & Myers (1995). This point, already made in Paper II, is strengthened by the larger sample and fully sampled maps presented here. Note that the "high-mass" regions of Caselli et al., observed toward Orion, cover a

TABLE 3
OBSERVED LINE PARAMETERS

Source	$I(T_R^*, CS)$[a] (K km s^{-1})	Δv(CS) (km s^{-1})	$I(T_R^*, C^{34}S)$[a] (K km s^{-1})	Δv(C^{34}S) (km s^{-1})	$I(T_R^*, {}^{13}CS)$[a] (K km s^{-1})	Δv(^{13}CS) (km s^{-1})
G121.30+0.66..................	22.2 (2.3)	3.46 (0.13)	1.5 (0.2)	4.23 (0.39)	...	...
G123.07−6.31..................	25.8 (2.7)	4.49 (0.13)	1.1 (0.2)	4.89 (0.45)	...	...
W3 (OH).........................	72.4 (7.3)	5.92 (0.13)	6.3 (0.7)	5.80 (0.18)	2.5 (0.3)	4.92 (0.25)
G135.28+2.80..................	6.5 (0.8)	3.46 (0.13)	...	...	...	...
S231	27.4 (2.8)	3.89 (0.13)	1.6 (0.2)	2.48 (0.19)	...	...
S235	32.0 (3.3)	2.68 (0.12)	2.9 (0.4)	2.09 (0.18)	0.5 (0.2)	2.32 (0.30)
S241	7.5 (0.9)	2.63 (0.14)	...	...	...	...
S252A	17.1 (1.8)	3.11 (0.12)	...	...	...	...
S255	47.8 (4.8)	3.12 (0.12)	...	...	...	...
RCW 142	116 (12)	6.00 (0.13)	26.2 (2.7)	5.60 (0.17)	12.8 (1.3)	5.52 (0.14)
W28A2 (1)	204 (20)	6.85 (0.15)	23.2 (2.3)	5.91 (0.15)	8.9 (0.9)	5.28 (0.16)
M8E..............................	32.5 (3.3)	3.12 (0.12)	4.7 (0.5)	2.23 (0.15)	...	...
G9.62+0.10	55.4 (5.6)	7.26 (0.19)	16.0 (1.6)	7.33 (0.38)	...	...
G8.67−0.36.....................	47.0 (4.8)	5.43 (0.15)	5.6 (0.6)	5.08 (0.27)	...	...
W31	55.9 (5.7)	11.11 (0.26)	7.3 (0.8)	8.56 (0.31)	...	...
G10.6−0.4	182 (18)	7.04 (0.13)	29.8 (3.0)	6.72 (0.14)	17.1 (1.7)	6.43 (0.13)
G12.42+0.50....................	24.8 (3.5)	3.13 (0.13)	...	...	...	...
G12.89+0.49....................	30.0 (3.1)	5.09 (0.13)	5.4 (0.5)	3.78 (0.14)	...	...
G12.2−0.1	35.0 (3.8)	8.01 (0.22)	4.2 (0.4)	7.06 (0.22)	...	...
W33 cont	122 (13)	6.49 (0.14)	21.1 (2.1)	5.13 (0.13)	10.8 (1.0)	4.72 (0.14)
G13.87+0.28....................	17.5 (1.9)	4.15 (0.18)	2.7 (0.3)	2.50 (0.21)	...	...
W33A	32.0 (3.3)	4.96 (0.18)	2.3 (0.3)	3.22 (0.27)	...	...
G14.33−0.64....................	53.6 (5.4)	4.97 (0.14)	4.5 (0.5)	2.74 (0.14)	...	...
G19.61−0.23....................	53.4 (5.8)	8.97 (0.23)	3.2 (0.4)	6.50 (0.30)	...	...
G20.08−0.13....................	26.7 (2.7)	8.20 (0.16)	4.5 (0.5)	8.39 (0.46)	...	...
G23.95+0.16....................	18.1 (1.9)	3.01 (0.13)	3.2 (0.4)	2.39 (0.25)	...	...
G24.49−0.04....................	17.3 (1.8)	4.43 (0.18)	...	...	...	...
W42	35.7 (3.7)	8.42 (0.19)	8.7 (0.9)	5.44 (0.13)	...	...
G28.86+0.07....................	16.3 (1.7)	5.34 (0.15)	2.5 (0.3)	3.17 (0.19)	...	...
W43S	52.6 (7.7)	5.01 (0.13)	8.0 (0.8)	3.97 (0.13)	...	...
G31.41+0.31....................	44.3 (4.5)	5.89 (0.24)	7.7 (0.8)	5.86 (0.20)	...	...
W43 Main 3	37.5 (4.1)	9.68 (0.12)	7.4 (0.8)	6.82 (0.23)	...	...
G31.44−0.26....................	22.7 (2.3)	5.22 (0.14)	2.0 (0.2)	3.80 (0.38)	...	...
G32.05+0.06....................	14.6 (1.5)	8.04 (0.18)	1.9 (0.2)	4.54 (0.59)	...	...
G32.80+0.20A/B	28.1 (2.9)	8.04 (0.14)	1.7 (0.3)	5.16 (0.74)	...	...
W44	107 (11)	5.92 (0.12)	21.8 (2.2)	5.04 (0.51)	7.6 (0.8)	4.72 (0.14)
S76E	56.3 (5.7)	3.70 (0.12)	...	...	...	...
G35.58−0.03....................	22.7 (2.5)	5.01 (0.18)	2.2 (0.4)	6.56 (0.52)	...	...
G35.20−0.74....................	31.8 (3.3)	6.49 (0.13)	1.9 (0.2)	8.45 (0.71)	...	...
W49N 4 km s^{-1}	103 (11)	9.79 (1.38)	2.2 (0.2)	9.80 (0.94)	1.4 (0.2)	9.14 (1.77)
W49N 12 km s^{-1}	63.4 (6.6)	9.54 (1.38)	3.0 (0.7)	5.60 (0.94)	3.8 (0.4)	7.38 (1.77)
W49S	27.3 (3.0)	8.32 (0.15)	1.9 (0.2)	7.56 (0.44)	...	...
OH 43.80−0.13	28.8 (2.9)	7.55 (0.23)	1.0 (0.1)	4.12 (0.30)	...	...
G45.07+0.13....................	42.3 (4.3)	6.08 (0.16)	7.8 (0.8)	6.10 (0.21)	...	...
G48.61+0.02....................	15.1 (1.6)	5.00 (0.17)	0.4 (0.1)	2.34 (0.24)	...	...
W51W	29.1 (3.3)	3.82 (0.14)	4.2 (2.0)	3.39 (0.28)	...	...
W51M	230 (23)	10.95 (0.13)	26.7 (2.7)	8.96 (0.18)	19.2 (1.9)	8.03 (0.19)
G59.78+0.06....................	17.4 (1.9)	3.20 (0.15)	0.6 (0.1)	1.11 (0.19)	...	...
S87	28.6 (3.0)	2.49 (0.16)	...	...	...	...
S88B	21.1 (2.2)	3.06 (0.13)	1.3 (0.1)	2.35 (0.18)	...	...
K3-50............................	25.2 (2.7)	8.07 (0.15)	1.4 (0.2)	7.61 (0.56)	...	...
ON 1	20.2 (2.1)	4.68 (0.13)	2.0 (0.3)	4.51 (0.24)	...	...
ON 2S	42.3 (4.4)	4.63 (0.13)	1.9 (0.2)	3.65 (0.18)	...	...
ON 2N	37.4 (3.8)	4.71 (0.13)	3.2 (0.3)	3.78 (0.10)	...	...
S106.............................	15.1 (1.7)	4.70 (0.17)	...	...	...	...
W75N	76.3 (7.7)	4.60 (0.12)	6.8 (0.7)	4.15 (0.15)	...	...
DR 21S	75.5 (7.6)	5.66 (0.15)	7.0 (0.7)	4.94 (0.15)	...	...
W75 (OH)	91.6 (9.2)	5.48 (0.12)	4.0 (0.4)	5.44 (0.18)	...	...
G97.53+3.19....................	11.8 (1.3)	6.76 (0.31)	...	...	...	...
BFS 11-B	7.8 (1.2)	3.14 (0.18)	...	...	...	...
Cep A............................	20.2 (2.2)	4.07 (0.16)	...	...	...	...
NGC 7538......................	72.5 (7.4)	5.65 (0.12)	5.2 (0.6)	4.39 (0.16)	...	...
S157.............................	20.4 (2.2)	3.51 (0.13)	...	...	...	...

[a] Peak position.

TABLE 4
OBSERVED PROPERTIES

Source	Centroid (arcsec)	R_{CS} (pc)	$(a/b)_{obs}$ [a]	P.A. (deg)	R_{10} [b] (pc)
G121.30+0.66..................	(−10, 0)	0.10 (0.01)	1.5	55	0.11 (0.01)
G123.07−6.31..................	(−10, 0)	0.14 (0.01)	1.7	110	0.16 (0.03)
W3 (OH).........................	(0, +10)	0.18 (0.01)	1.4	60	0.5 (0.01)
G135.28+2.80..................	(0, +10)	0.10 (0.09)	1.5	50	U
S231	(0, −10)	0.17 (0.01)	1.2	135	0.24 (0.03)
S235	(0, 0)	0.15 (0.01)	M	...	0.21 (0.01)
	(0, −70)	...	M	...	...
S241	(0, +10)	0.23 (0.05)	1.7	90	U
S252A	(−10, +10)	0.10 (0.01)	1.2	135	U
	(+60, −60)	...	M	...	...
S255	(0, 0)	...	M	...	M
RCW 142	(0, 0)	0.14 (0.01)	1.2	120	E
W28A2 (1)	(−10, 0)	0.15 (0.04)	1.1	125	E
M8E..............................	(0, 0)	0.14 (0.01)	1.3	115	0.18 (0.02)
G9.62+0.10	(−10, +10)	0.33 (0.01)	1.3	35	0.56 (0.05)
G8.67−0.36.....................	(0, +10)	0.26 (0.01)	1.2	35	0.43 (0.04)
W31	(−10, +10)	0.67 (0.04)	1.6	0	1.37 (0.11)
G10.6−0.4	(0, +10)	0.41 (0.01)	1.0	45	E
G12.42+0.50....................	(0, 0)	...	M	...	M
	(+10, +40)	...	M	...	...
G12.89+0.49....................	(0, 0)	0.19 (0.01)	1.3	115	0.24 (0.04)
G12.2−0.1	(0, +10)	0.65 (0.08)	1.2	25	0.97 (0.20)
W33 cont	(+10, +10)	0.75 (0.02)	1.0	...	E
G13.87+0.28....................	(0, 0)	0.33 (0.03)	1.2	120	U
W33A	(+10, +10)	0.26 (0.01)	1.0	...	0.35 (0.04)
G14.33−0.64....................	(0, 0)	0.17 (0.01)	1.1	140	0.29 (0.02)
G19.61−0.23....................	(0, 0)	0.20 (0.02)	1.2	140	0.31 (0.06)
G20.08−0.13....................	(+10, 0)	0.15 (0.01)	1.1	150	0.19 (0.04)
G23.95+0.16....................	(+10, 0)	0.45 (0.03)	1.3	55	U
G24.49−0.04....................	(−10, +10)	0.17 (0.01)	1.0	...	U
W42	(−10, 0)	0.49 (0.04)	1.0	...	0.64 (0.11)
G28.86+0.07....................	(0, +10)	0.47 (0.02)	1.3	25	U
W43S	(0, +10)	0.46 (0.03)	1.4	160	E
G31.41+0.31....................	(0, 0)	0.36 (0.02)	1.1	90	0.56 (0.10)
W43 Main 3	(0, 0)	0.52 (0.05)	1.5	60	1.00 (0.08)
G31.44−0.26....................	(0, 0)	0.52 (0.03)	1.0	...	0.54 (0.13)
G32.05+0.06....................	(0, 0)	0.48 (0.02)	1.1	40	U
G32.80+0.20A/B	(−10, 0)	0.96 (0.06)	1.1	55	1.18 (0.17)
W44	(0, 0)	0.37 (0.01)	1.2	45	E
S76E	(0, 0)	0.20 (0.01)	1.6	130	0.37 (0.01)
G35.58−0.03....................	(0, 0)	0.20 (0.02)	1.1	140	0.21 (0.06)
G35.20−0.74....................	(0, −10)	0.30 (0.02)	1.4	35	0.45 (0.03)
W49N 4 km s^{-1}	(−10, 0)	1.41 (0.04)	...	...	E
W49N 12 km s^{-1}	(−20, 0)	...	M	...	M
	(+10, +20)	...	M	...	...
W49S	(0, 0)	1.53 (0.13)	M	...	M
	(−20, +60)	...	M	...	...
OH 43.80−0.13	(0, −10)	0.11 (0.01)	1.4	125	0.15 (0.03)
G45.07+0.13....................	(0, 0)	0.48 (0.02)	...	...	0.70 (0.11)
G48.61+0.02....................	(0, 0)	0.54 (0.06)	1.3	145	E
W51W	(−20, 0)	0.64 (0.08)	1.6	110	0.82 (0.19)
W51M	(0, 0)	0.50 (0.01)	M	...	M
	(−70, +40)	...	M	...	...
G59.78+0.06....................	(−10, +20)	0.18 (0.01)	M	...	U
S87................................	(0, 0)	...	M	...	M
	(+10, +60)	...	M	...	...
S88B	(+20, 0)	0.16 (0.01)	1.0	...	0.17 (0.02)
K3-50............................	(0, +10)	0.71 (0.05)	1.3	50	0.83 (0.12)
ON 1	(0, 0)	0.43 (0.03)	1.0	...	0.43 (0.09)
ON 2S	(−10, −10)	0.61 (0.02)	1.8	55	0.87 (0.05)
ON 2N	(0, 0)	0.41 (0.02)	1.2	40	0.64 (0.05)
S106	(+10, 0)	0.37 (0.06)	...	...	U
W75N	(0, 0)	0.27 (0.01)	1.5	70	0.63 (0.02)
DR 21S	(0, 0)	0.27 (0.01)	M	...	M

TABLE 4—*Continued*

Source	Centroid (arcsec)	R_{CS} (pc)	$(a/b)_{obs}$ [a]	P.A. (deg)	R_{10} [b] (pc)
	$(-60, 0)$	. . .	M	. . .	. . .
W75 (OH)	$(0, 0)$	0.29 (0.01)	1.5	60	M
G97.53+3.19....................	$(+10, 0)$	. . .	M	. . .	M
	$(0, -20)$	. . .	M	. . .	. . .
BFS 11-B	$(0, 0)$	0.12 (0.03)	. . .	. . .	U
Cep A..............................	$(-10, -10)$	. . .	M	. . .	M
	$(+10, +10)$	. . .	M	. . .	. . .
NGC 7538.......................	$(0, 0)$	0.32 (0.01)	M	. . .	M
	$(0, +80)$	. . .	M	. . .	. . .
S157	$(0, +10)$	0.19 (0.01)	1.0	. . .	0.19 (0.03)

[a] M = Multiple cores resulting in ambiguity.
[b] E = Contour extended beyond map boundary, U = unresolved.

similar range of radii but are less massive than those studied here. Extension of the line width–size relation found in previous studies to regions of massive star formation would be very misleading.

We attribute the large line widths to turbulent motions since the thermal contribution to the line width is negligible. Assuming $T_k = 50$ K, thermal broadening accounts for only 0.23 km s^{-1}, whereas the smallest line width in our sample is 2.49 km s^{-1} (S87). The sonic line width for $T_k = 50$ K gas and a mean molecular weight of $\mu = 2.29$ is 1.0 km s^{-1}. Outflows are apparent in line wings for some sources, but they are unlikely to broaden the FWHM line width, except by stirring up turbulence. The turbulent line width of this sample is highly supersonic. Our regions are at least 4 times more turbulent than regions involved in lower mass star formation (see Mardones et al. 1997; Gregersen et al. 1997). Based on comparison of power-law models using dust emission, Mueller et al. (2002b) found that these cores were also about 100 times denser on average than the low-mass sample.

4.3. *Virial Mass*

The virial mass for a homoeoidal ellipsoid (concentric ellipsoids of revolution with equal aspect ratios) is given by

$$M_{vir}(R) = \frac{5R\Delta v^2}{8a_1 a_2 G \ln 2} \approx 209 \frac{(R/1 \text{ pc})(\Delta v/1 \text{ km s}^{-1})^2}{a_1 a_2} M_\odot;$$

(7)

$$a_1 = \frac{1 - p/3}{1 - 2p/5}, \quad p < 2.5 .$$

(8)

where a_1 is the correction for a power-law density distribution and a_2 is the correction for a nonspherical shape (Bertoldi & McKee 1992). For aspect ratios less than 2, $a_2 \sim 1$ and can be ignored for our sample. The equation in Bertoldi & McKee uses an rms velocity; we have converted to the observable (Δv) under the assumption that turbulent broadening dominates thermal broadening; this is a very safe assumption for these sources, but it fails for lines of light species in very quiescent regions (see Shirley et al. 2002b).

There are several corrections used in calculating the virial mass. Since the CS line width was found to be optically thick in some cores, we use the C^{34}S line width when it was observed. The remaining cores (7) are corrected using the average ratio of C^{34}S to CS line width for the sample (§ 4.2). We use the density power-law index, p, from Mueller et al. (2002b) for the cores common to each sample (21) and use the average $p = 1.77$ for the remaining cores. Finally, we must choose a radius within which to calculate the virial mass. Initially, we use R_{CS}. However, since a power-law density distribution has no characteristic size, we also calculate virial masses using R_n, the radius at which the density of
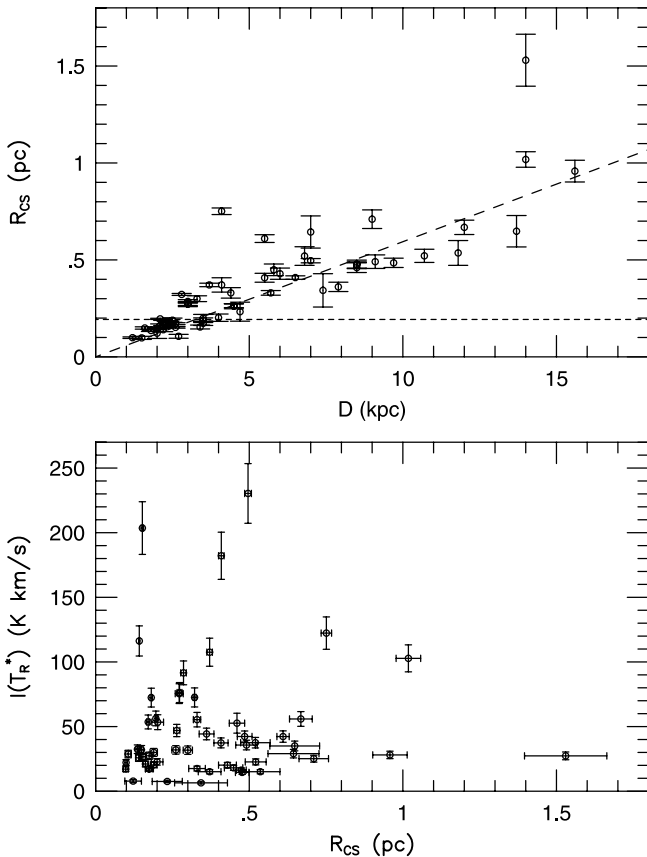

FIG. 14.—Plot of core size vs. distance (*upper panel*) and integrated intensity vs. R_{CS} (*lower panel*). The dashed line in the upper panel shows the size of a core with a deconvolved size equal to the beam size, while the horizontal dashed line marks the source size with a deconvolved source size equal to the beam for the median distance of the sample. No correlation is observed between integrated intensity and R_{CS}.
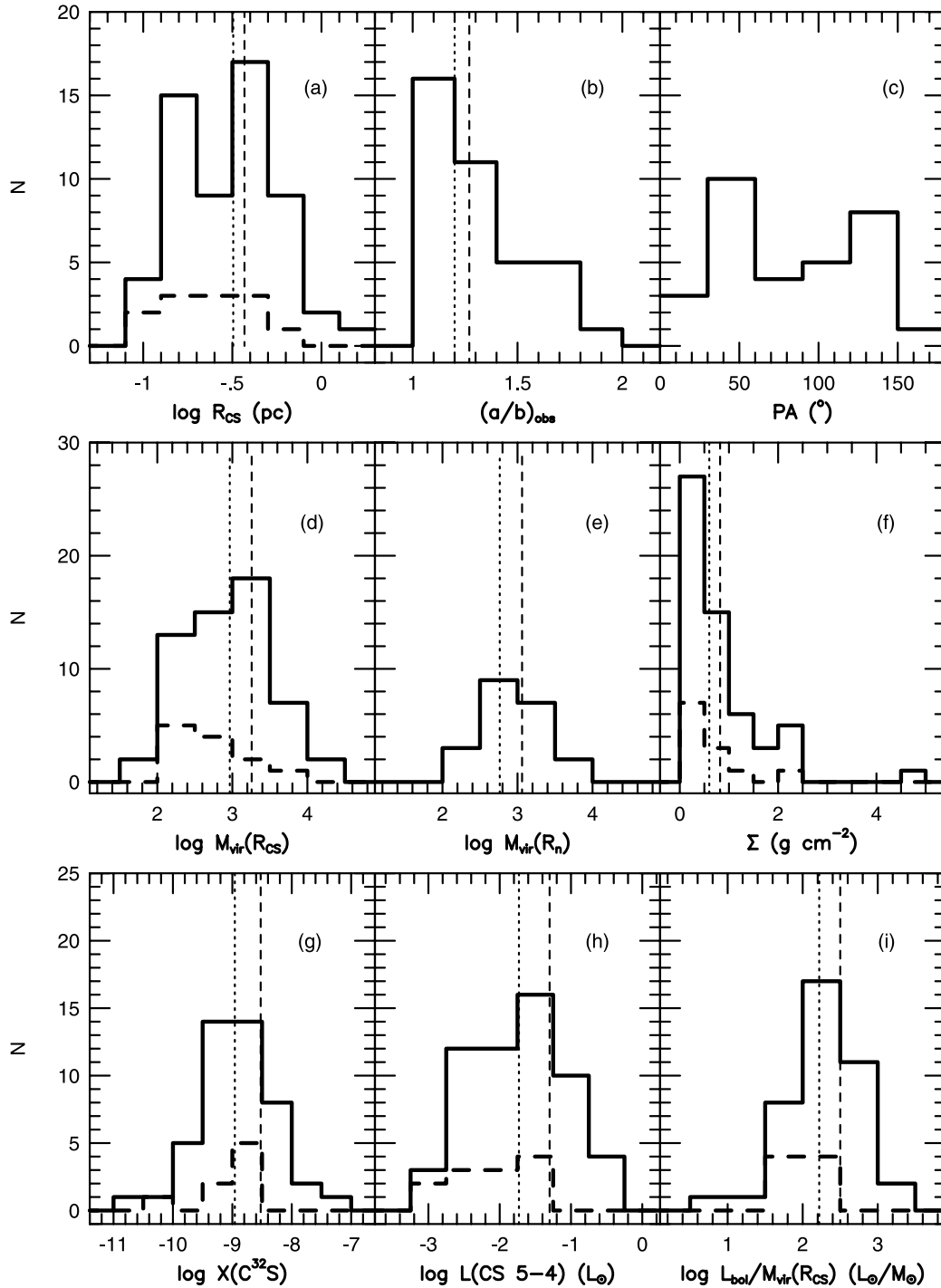
FIG. 15.—Histograms of R_{CS}, $(a/b)_{obs}$, major-axis position angle, M_{vir}, Σ, CS abundance, CS $J = 5 \rightarrow 4$ luminosity, and L_{bol}/M_{vir}. Distributions of sources without a known radio continuum detection are plotted as dashed-line histograms (panels a, d, f, g, h, and i). The total distributions (including all sources) are plotted as solid-line histograms. The mean (*dashed vertical line*) and median (*dotted vertical line*) of the total distributions are plotted.

the dust models drops to 10^4 cm^{-3} (Mueller et al. 2002b). This density corresponds to the density of the ambient molecular cloud at the edge of a core based on a detailed study of molecular clouds in our Galaxy (K. N. Allers et al. 2003, in preparation). The average $R_n = 0.40$ pc is only slightly larger than the average R_{CS}. The virial mass using corrections for $\langle p \rangle$ and $\langle \Delta v(C^{34}S)/\Delta v(C^{32}S) \rangle$ is 2.3 times smaller than the mass calculated using $\Delta v(C^{32}S)$ and assum-

ing a constant density envelope. It is crucial to account for variations in density structure and optical depth effects when calculating the virial mass.

The distributions of virial masses are peaked near 1000 $M_\odot$, for either definition of the cloud radius (Figs. 15d and 15e). Only cores for which all the corrections could be made (21) are included in the $M_{vir}(R_n)$ histogram. Our sample begins to be incomplete for cores with masses less than

TABLE 5
DERIVED PROPERTIES

Source	p^a	$M_{\rm vir}(R_{\rm CS})$ ($M_\odot$)	$M_{\rm vir}(R_n)$ ($M_\odot$)	Σ (g cm^{-2})	$\log X$(CS)	L(CS 5–4) ($10^{-2} L_\odot$)	$L_{\rm bol}/M_{\rm vir}$ $(L/M)_\odot$
G121.30+0.66	1.25	320 (80)	1870	2.16 (0.59)	−10.53 (0.13)	0.10 (0.03)	3
G123.07−6.31	1.75	500 (200)	1640	1.72 (0.73)	. . .	0.28 (0.09)	12
W3 (OH)	1.50	1020 (130)	3550	2.08 (0.29)	−9.57 (0.36)	1.15 (0.27)	93
G135.28+2.80	. . .	210 (110)	. . .	0.12 (0.09)	−8.86 (0.42)	0.60 (0.34)	269
S231	1.50	180 (50)	490	0.40 (0.12)	−8.74 (0.41)	0.40 (0.13)	73
S235	. . .	100 (40)	. . .	0.29 (0.11)	−9.43 (0.12)	0.30 (0.08)	98
S241	. . .	140 (60)	. . .	0.18 (0.11)	. . .	0.30 (0.16)	91
S252A	1.75	140 (90)	350	0.99 (0.67)	. . .	0.09 (0.03)	45
RCW 142	2.25	370 (290)	610	1.23 (0.95)	−8.28 (1.37)	1.19 (0.27)	153
W28A2 (1)	2.25	450 (340)	1280	1.29 (0.97)	−7.78 (3.75)	2.85 (0.65)	450
M8E	1.75	100 (30)	200	0.37 (0.11)	−8.14 (0.89)	0.29 (0.07)	166
G9.62+0.10	2.00	2230 (870)	3930	1.37 (0.54)	−8.50 (0.89)	3.68 (0.87)	157
G8.67−0.36	2.00	860 (340)	1890	0.82 (0.33)	. . .	1.97 (0.47)	152
W31	. . .	7300 (1670)	. . .	1.09 (0.28)	−8.44 (0.64)	15.9 (4.1)	. . .
G10.6−0.4	2.50	2750 (460)	. . .	1.10 (0.19)	−7.90 (2.44)	17.2 (3.9)	334
G12.89+0.49	2.00	340 (130)	470	0.63 (0.25)	−9.08 (0.29)	0.71 (0.19)	115
G12.2−0.1	. . .	4810 (1480)	. . .	0.77 (0.30)	−8.83 (0.59)	11.3 (3.9)	114
W33 cont	. . .	2950 (520)	. . .	0.35 (0.06)	−8.27 (0.69)	22.7 (5.7)	. . .
G13.87+0.28	1.75	310 (120)	350	0.19 (0.08)	−8.60 (0.46)	0.92 (0.32)	419
W33A	1.50	454 (130)	1260	0.44 (0.13)	. . .	1.33 (0.34)	220
G14.33−0.64	2.00	160 (60)	450	0.37 (0.14)	−8.48 (0.39)	0.85 (0.20)	621
G19.61−0.23	. . .	1270 (380)	. . .	2.08 (0.73)	−9.19 (0.39)	1.55 (0.48)	141
G20.08−0.13	. . .	1610 (460)	. . .	4.56 (1.42)	−9.83 (0.45)	0.51 (0.13)	. . .
G23.95+0.16	1.50	430 (150)	270	0.14 (0.05)	. . .	1.72 (0.55)	443
G24.49−0.04	2.25	300 (130)	450	0.67 (0.31)	−8.98 (0.67)	0.38 (0.10)	164
W42	. . .	2160 (480)	. . .	0.60 (0.16)	−8.78 (0.39)	5.66 (1.59)	. . .
G28.86+0.07	. . .	710 (200)	. . .	0.21 (0.06)	−8.71 (0.46)	2.33 (0.55)	. . .
W43S	2.50	1080 (230)	. . .	0.34 (0.08)	−8.97 (0.45)	7.31 (2.01)	1480
G31.41+0.31	2.25	1040 (930)	2090	0.53 (0.48)	−9.16 (0.39)	4.62 (1.17)	221
W43 Main 3	. . .	3610 (960)	. . .	0.89 (0.29)	. . .	4.84 (1.88)	. . .
G31.44−0.26	. . .	1120 (490)	. . .	0.28 (0.13)	−9.12 (0.38)	4.56 (1.18)	. . .
G32.05+0.06	. . .	1470 (790)	. . .	0.43 (0.23)	−8.81 (0.63)	2.09 (0.52)	. . .
G32.80+0.20A/B	. . .	3800 (2280)	. . .	0.28 (0.17)	−8.68 (0.62)	14.8 (4.07)	. . .
W44	. . .	1400 (600)	. . .	0.68 (0.29)	−8.92 (0.67)	5.95 (1.45)	214
S76E	1.50	240 (20)	. . .	0.41 (0.04)	−8.39 (0.58)	0.90 (0.21)	118
G35.58−0.03	. . .	1280 (500)	. . .	2.15 (0.93)	−9.40 (0.49)	0.56 (0.19)	33
G35.20−0.74	. . .	3200 (1190)	. . .	2.37 (0.90)	−9.35 (0.69)	1.22 (0.35)	. . .
W49N 4km s^{-1}	. . .	14570 (5960)	. . .	0.94 (0.39)	−8.56 (0.62)	52.8 (13.4)	. . .
W49S	. . .	13030 (4140)	. . .	0.37 (0.13)	−8.61 (0.32)	17.9 (7.2)	. . .
OH 43.80−0.13	. . .	270 (100)	. . .	1.59 (0.66)	−9.14 (0.34)	0.32 (0.08)	. . .
G45.07+0.13	. . .	2690 (580)	. . .	0.77 (0.18)	−9.02 (0.46)	7.14 (1.73)	446
G48.61+0.02	. . .	440 (200)	. . .	0.10 (0.06)	−8.37 (0.51)	3.50 (1.13)	2290
W51W	. . .	1100 (480)	. . .	0.18 (0.09)	−9.32 (0.32)	3.81 (1.85)	. . .
W51M	. . .	5930 (980)	. . .	1.61 (0.28)	−8.40 (1.45)	28.7 (6.6)	472
G59.78+0.06	. . .	30 (20)	. . .	0.07 (0.05)	−8.13 (0.56)	0.25 (0.09)	. . .
S88B	1.25	160 (40)	220	0.41 (0.10)	−9.26 (0.18)	0.26 (0.07)	562
K3-50	. . .	6130 (2140)	. . .	0.81 (0.30)	−10.15 (1.19)	5.92 (1.91)	343
ON 1	1.75	1320 (370)	2230	0.48 (0.15)	. . .	1.87 (0.58)	114
ON 2S	1.75	1220 (300)	700	0.22 (0.06)	−9.33 (0.30)	6.02 (1.60)	302
ON 2N	. . .	870 (210)	. . .	0.35 (0.09)	. . .	3.04 (0.88)	. . .
S106	. . .	720 (180)	. . .	0.35 (0.11)	. . .	0.88 (0.39)	692
W75N	. . .	700 (180)	. . .	0.63 (0.13)	−9.59 (0.41)	2.41 (0.60)	. . .
DR 21S	. . .	990 (220)	. . .	0.90 (0.22)	−9.79 (0.32)	1.78 (0.48)	506
W75 (OH)	. . .	1260 (250)	. . .	1.03 (0.21)	−9.41 (0.34)	2.30 (0.56)	40
BFS 11-B	. . .	110 (50)	. . .	0.48 (0.31)	. . .	0.07 (0.05)	66
NGC 7538	. . .	920 (190)	. . .	0.60 (0.12)	−9.39 (0.09)	2.83 (0.66)	206
S157	0.75	200 (20)	450	0.39 (0.06)	−9.91 (1.05)	0.35 (0.10)	141

^{a} $p = -\log n / \log r$ from Mueller et al. 2002b.

about 10^3 $M_\odot$ because they will tend to be too small to resolve at the average distance of sources in our sample (5.3 kpc). Consequently, the peaked histograms and the average values given below should be taken only as representative of this particular sample. A weak correlation is observed between $\log M_{\rm vir}$ and $\log I(T_R^*)$ ($r = 0.43$), indicating that more massive cores are typically brighter in CS emission (Fig. 19).
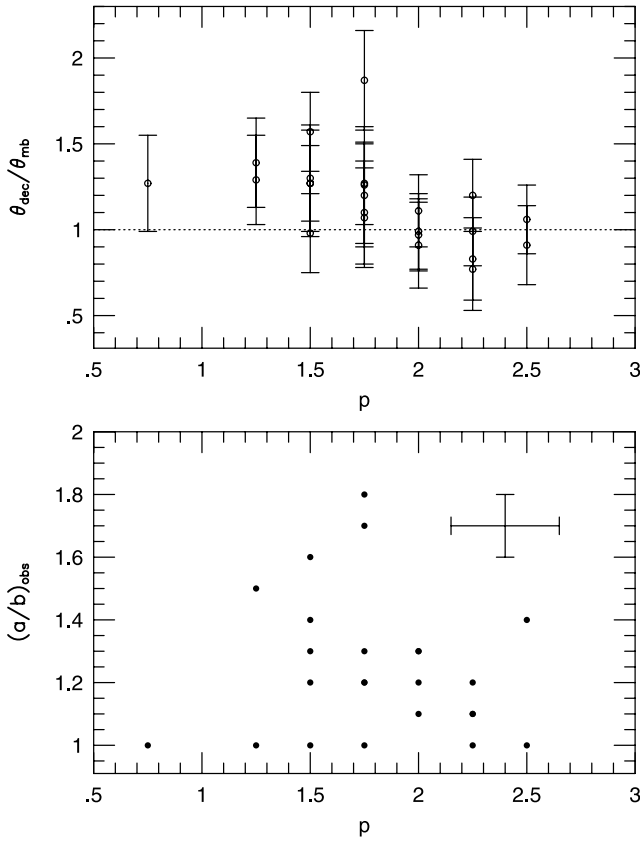
FIG. 16.—Aspect ratio (*lower panel*) and the deconvolved source size (θ_{dec}/θ_{mb}; *upper panel*) are compared with the best-fit power-law density index determined by Mueller et al. (2002b). No correlation between aspect ratio and p is observed, while a weak correlation is observed between p and θ_{dec}/θ_{mb}. The typical error bars for $(a/b)_{obs}$ and p are shown in the bottom panel.

FIG. 17.—Upper panel shows the CS line width compared with $C^{34}S$ line width. For the subsample of cores mapped in both CS and $C^{34}S$, the CS line width is broader on average. Lower panel shows the $C^{34}S$ and ^{13}CS line widths.

The median virial mass using R_{CS} is 920 $M_\odot$ for the full sample of 57 cores. The large dispersion about the mean mass ($\pm 2810\ M_\odot$, see Table 6) partially results from the mass of W49N, which is 8 times higher than the average mass; therefore, the median is a better indicator of the typical virial mass for this sample. Sources without known radio continuum emission ($N = 12$) have a smaller median virial mass of 329 $M_\odot$. As was found for the size distributions, there is no statistically significant difference between the median virial masses of sources with UCH II, CH II, or H II regions and the complete sample. The median virial mass using R_n is 610 $M_\odot$ using the subsample of 21 cores that were modeled by Mueller et al. (2002b).

The virial mass may be compared with the mass derived from models of the dust continuum emission at 350 μm, denoted $M_{dust}(R_{CS})$ (Mueller et al. 2002b), for the sources in common. The average ratio of virial mass to dust-determined mass ($\langle M_{vir}/M_{dust}\rangle$) is 3.4 ± 3.3, and the median ratio is 2.2 for 21 sources with virial mass corrections, $C^{34}S$ line widths, and dust models (see Fig. 19). Given the many sources of uncertainty in deriving virial and dust-determined masses (distance, dust opacity, etc.), the agreement is good. The agreement suggests that the assumptions used in deriving the virial mass and the choice of Ossenkopf & Henning (1994) opacities for the dust are sensible and that virial masses provide a good mass estimate.

Since the regions we are studying are forming massive stars, we can compare the virial mass with regions that have formed high-mass stars, namely OB associations. Matzner (2002) calculated a mean mass per association of 440 $M_\odot$ based on the Galactic H II region luminosity function of McKee & Williams (1997). This mass is roughly 50% of the median virial mass calculated using R_{CS} and 75% of the virial mass calculated using R_n. If the regions traced by water maser emission and CS $J = 5 \rightarrow 4$ emission are forming a single new OB association, then the star formation efficiency of the gas traced by high-J CS emission is high ($\sim 50\%$). However, this star formation efficiency is an upper limit if more than one dense core contributes to the formation of a new OB association.

4.4. *The Mass Spectrum*

Because all these cores have masses greater than those of individual stars, they are destined to form clusters or associations. The cumulative mass spectrum of dense cores should then be directly related to the cumulative distribution of the *total* mass of stars in clusters or OB associations [$M_*(tot)$]. Using the model of McKee & Williams (1997), the cumulative distribution of $M_*(tot)$ in OB associations is proportional to $M_*(tot)^{-1}$. The mass function of our cores may be related less directly to the initial mass function of stars *within* those clusters and associations (the usual IMF). Stars above about 5 $M_\odot$ roughly follow a power-law mass spectrum [$N(> M) \propto M^\Gamma$], with Γ often assumed to be -1.35
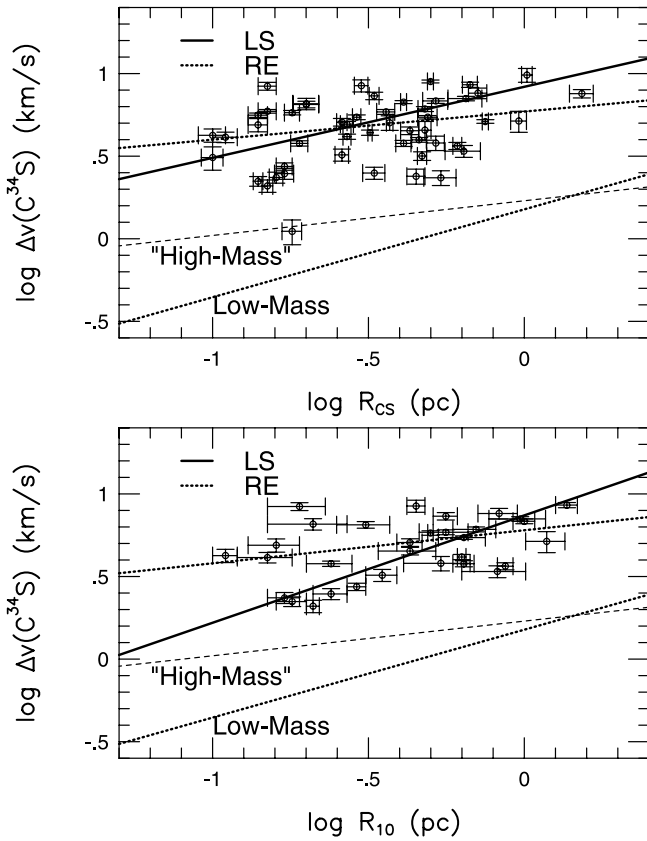
FIG. 18.—Line width–size relationship using $C^{34}S$ line widths. The FWHM size, R_{CS}, is shown in the top panel, and the size at an intensity of 10 K km s^{-1}, R_{10}, is shown in the bottom panel. The extrapolated line width–size relationships for low- and high-mass regions are labeled, and the least-squares fit and robust estimation for our sample are shown.

FIG. 19.—Logarithm of $I(T_R^*)$ and log M_{vir} are compared in the upper panel and the virial mass and dust-determined mass are compared in the lower panel. More massive cores are typically brighter in CS intensity: $\log I(T_R^*) = (-0.76 \pm 0.11) + (0.81 \pm 0.04) \log M_{vir}$. The virial mass and mass derived from dust continuum emission correlate well, but $M_{vir} > M_{dust}$. The solid line in the top panel is the least-squares fit, while the solid line in the bottom panel indicates $M_{vir} = M_{dust}$.

(Salpeter 1955). Massey et al. (1995) find $\Gamma = -1.1 \pm 0.1$(standard deviation of the mean) for 13 OB associations. In contrast to these slopes, molecular clouds as a whole have a flatter distribution. Mass spectra with Γ of -0.6 to -0.7 have been observed for molecular clouds (see Scoville & Sanders 1987), as well as the large clumps within clouds (Blitz 1993; Williams, Blitz, & McKee 2000; Kramer et al. 1998). Studies of cores forming low-mass stars in Ophiuchus reveal a steeper mass spectrum, $\Gamma = -1.5$ (Motte, André, & Neri 1998; Johnstone et al. 2000), and a study in Serpens finds $\Gamma = -1.1$ (Testi & Sargent 1998). These slopes begin to resemble the slope of the IMF for massive stars, but they mostly apply to lower mass regions where the stellar IMF actually turns over (Scalo 1998; Meyer et al. 2000).

The cumulative mass spectrum of cores, based on the corrected virial masses, is shown in Figure 20. The mass spectrum is clearly incomplete below about 1000 $M_\odot$. The spectrum for $M_{vir} \geq 1000$ $M_\odot$ was fitted using least-squares and robust estimation (Fig. 20), with resulting $\Gamma = -0.91 \pm 0.17$ and $\Gamma = -0.95$, respectively. The mass function of dense cores is similar to that of M_*(tot) in the model of McKee & Williams (1997). It is also within the range of the values for the IMF of stars within OB associations (Massey et al. 1995). The similarity of our value for Γ to that of the IMF of stars within clusters suggests that the fragmentation process keeps nearly the same mass spectrum.

Our mass spectrum is slightly steeper than found by other studies toward high-mass star-forming regions that used

probes that trace lower densities. Kramer et al. (1998) find $\Gamma = -0.6$ to -0.8 for CO clumps within seven high-mass star-forming clouds. A CS $J = 2 \rightarrow 1$ survey toward 55 dense cores containing water masers found $\Gamma = -0.6 \pm 0.3$ (Zinchenko et al. 1998).

4.5. Surface Density, Pressure, and Confinement of UCH II Regions

McKee & Tan (2002, 2003) have emphasized the importance of the surface density of a molecular core (which they call a clump) in the stellar mass accretion rate ($dm_*/dt \propto \Sigma^{0.75}$) and the time to form a star ($t_{*f} \propto \Sigma^{-0.75}$). Based on the results in Paper II, they assumed $\Sigma = 1.0$ g cm^{-2}.

The surface density of the core can be calculated from

$$\Sigma = \frac{M_{vir}(R_{CS})}{\pi R_{CS}^2} \approx 0.665 \frac{(M_{vir}/1.0 \times 10^4 \ M_\odot)}{(R_{CS}/1 \text{ pc})^2} \text{ g cm}^{-2} . \quad (9)$$

The average over the sample with well-determined sizes is $\Sigma = 0.82 \pm 0.78$ g cm^{-2} with a median of 0.60 g cm^{-2}. The median surface density corresponds to 2870 $M_\odot$ pc^{-2}. The surface densities range from 0.07 g cm^{-2} (G58.78+0.06) to 4.6 g cm^{-2} (G20.08$-$0.13). While the distribution is sharply peaked for $\Sigma < 1$ g cm^{-2}, a few cores (6) have surface densities greater than 2 g cm^{-2} (Fig. 15f). The median surface density would imply a decrease in the mass accretion rate and increase in the star formation time for the accretion

TABLE 6
STATISTICAL SUMMARY

Source Property	Sample[a]	N	Mean	Standard Deviation	Mean Deviation[b]	Median	Skewness[c]	Units
D	Total	63	5.3	3.7	3.0	4.0	1.1	kpc
D_g	Total	63	7.2	2.6	2.2	6.8	0.5	kpc
$I_{peak}(T_R^*, CS)$	Total	63	47.2	44.7	30.1	31.8	2.4	K km s^{-1}
	NoRC	12	25.9	23.1	14.8	19.7	2.3	K km s^{-1}
	UCH II	32	50.4	41.0	29.1	35.7	2.1	K km s^{-1}
	CH II/H II	19	54.6	58.0	37.7	32.0	2.3	K km s^{-1}
$(S/N)_{peak}$	Total	63	50	40	27	40	2.4	
$I_{peak}(T_R^*, C^{34}S)$	Total	49	6.5	7.5	5.2	4.0	1.9	K km s^{-1}
R_{CS}	Total	57	0.37	0.26	0.19	0.32	2.0	pc
	NoRC	12	0.28	0.14	0.12	0.25	0.6	pc
	UCH II	27	0.38	0.32	0.22	0.27	2.2	pc
	CH II/H II	18	0.43	0.22	0.17	0.41	0.7	pc
R_{10}	Total	33	0.50	0.32	0.26	0.43	0.9	pc
$\Delta v(C^{32}S)$	Total	63	5.6	2.2	1.8	5.1	0.7	km s^{-1}
$\Delta v(C^{34}S)$	Total	51	5.0	2.0	1.7	4.9	0.4	km s^{-1}
$\Delta v(^{13}CS)$	Total	9	5.7	2.0	1.5	5.3	0.3	km s^{-1}
$(a/b)_{obs}$	Total	47	1.27	0.22	0.18	1.20	0.6	
$M_{vir}(R_{CS})$	Total	57	1810	2810	1750	920	3.1	$M_\odot$
	NoRC	12	760	1000	678	330	2.5	$M_\odot$
	UCH II	27	2170	3650	2200	990	2.8	$M_\odot$
	CH II/H II	18	1960	1990	1650	1160	1.1	$M_\odot$
$\log M_{vir}(R_{CS})$	Total	57	2.90	0.57	0.46	2.97	0.04	$\log M_\odot$
$M_{vir}(R_n)$	Total	21	1180	1080	870	610	1.3	$M_\odot$
$\Sigma(R_{CS})$	Total	57	0.82	0.78	0.55	0.60	2.4	g cm^{-2}
$f_v(p=0)$	Total	42	0.47	0.72	0.50	0.14	2.4	
$X(CS)$	Total	46	3.0	5.9	3.1	1.1	4.4	10^{-9}
$\log X(CS)$	Total	46	−8.93	0.62	0.49	−8.94	−0.1	
$L(CS54)$	Total	57	5.0	8.8	5.2	1.9	3.6	$10^{-2} L_\odot$
$\log L(CS54)$	Total	57	−1.8	0.7	0.5	−1.7	0.01	$\log L_\odot$
$L_{bol}/M_{vir}(R_{CS})$	Total	40	310	420	250	160	3.4	$(L/M)_\odot$
	NoRC	9	120	90	70	90	0.7	$(L/M)_\odot$
	UCH II	15	300	220	200	170	0.6	$(L/M)_\odot$
	CH II/H II	16	440	600	370	260	2.5	$(L/M)_\odot$
$\log L_{bol}/M_{vir}(R_{CS})$	Total	40	2.24	0.52	0.38	2.22	−0.8	$\log (L/M)_\odot$
$\langle \bar{P}/k \rangle$	Total	57	5.4	12.6	6.3	1.5	5.4	10^8 K cm^{-3}
$\log \langle \bar{P}/k \rangle$	Total	57	8.14	0.76	0.61	8.18	−0.1	$\log$ K cm^{-3}

[a] Distribution sample. Total = complete sample. NoRC = no known radio continuum. UCH II = contains UCH II region. CH II/H II = associated with CH II or H II region.

[b] Mean deviation = $(1/N) \sum_i |x_i - \langle x \rangle|$.

[c] Skewness = $\sum_i (x_i - \langle x \rangle)^3 / [(N-1)\sigma^3]$.

models of McKee & Tan (2002, 2003) by a factor of 2/3. The picture of McKee & Tan would imply that cores with higher Σ should have a higher star formation rate. Then one might expect the luminosity to correlate with Σ. We see no correlation ($r = -0.06$) in our data, but the range of Σ is small.

The large surface densities and line widths also translate into high pressures, both thermal and turbulent. Using equation (A6) from McKee & Tan (2003),

$$\langle \bar{P}/k \rangle \approx 4.25 \times 10^8 (\Sigma/1 \text{ g cm}^{-2})^2 \text{ K cm}^{-3}, \quad (10)$$

we compute a mean pressure for each of our cores with a known surface density. The average over these cores is $\langle \bar{P}/k \rangle = (5.4 \pm 12.6) \times 10^8$ K cm^{-3}, with a median value of 1.5×10^8 K cm^{-3}. The distribution is highly skewed by the core with very high surface density, so the median is more representative.

These high pressures may have some bearing on the issue of confinement of UCH II regions (see De Pree, Rodriguez,

& Goss 1995). Simple considerations suggest that the thermal pressure of a UCH II with $T_e = 10^4$ K and $n_e = 10^4$ cm^{-3} could be balanced by the median pressure in these cores. The pressure would be even higher close to the center of the cores. Mueller et al. (2002b) found a median density over 1.4×10^7 cm^{-3} at the fiducial radius of 1000 AU, and a median temperature of 260 K, leading to a thermal pressure of 4×10^9 K cm^{-3}. Including turbulent pressure raises this to about 1.5×10^{10} K cm^{-3}, comparable to those in the newly discovered hypercompact H II regions, which have sizes on the order of 1000 AU (e.g., Kurtz & Franco 2002).

While the issues surrounding UCH II regions are complicated (see Kurtz et al. 2000 for a review), our data do generally agree with the idea that turbulent pressure in the surrounding molecular gas may affect the evolution of H II regions (Xie et al. 1996). Xie et al. have suggested an anticorrelation between the turbulent line width and the size of a UCH II region for a sample of eight sources. We do not find strong evidence for an anticorrelation ($r = -0.29$) between $\Delta v(C^{34}S)$ ($r = -0.12$) or $\langle \bar{P}/k \rangle$ ($r = -0.29$) and
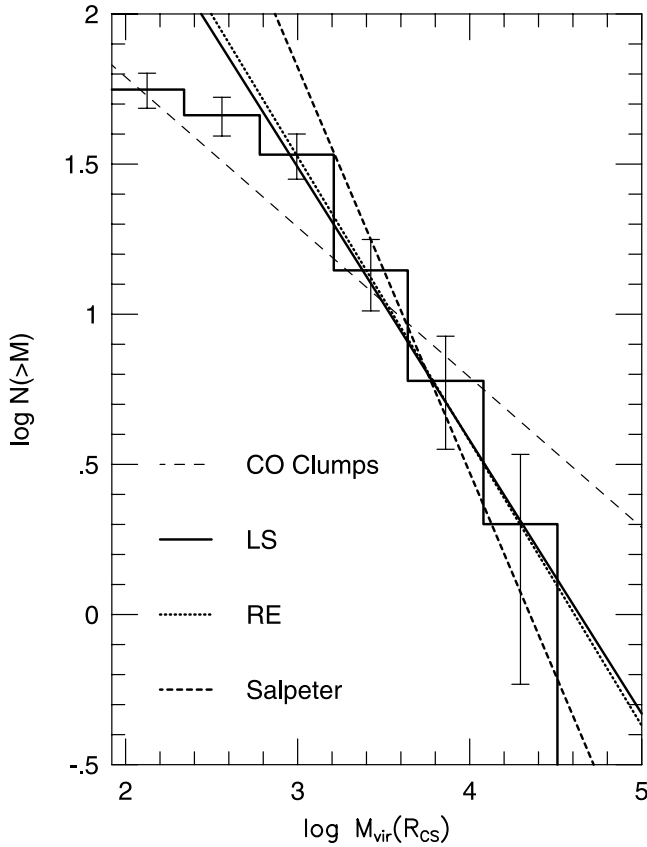
FIG. 20.—Cumulative mass spectrum determined from the CS core virial mass. Least-squares and robust estimation fits are shown as well as the Salpeter IMF and CO clump mass slope.

UCH II region sizes (Table 1); however, the line width and mean pressure determined from CS $J = 5 \rightarrow 4$ observations with a large beam size is probably not the best tracer of the gas that may be directly associated with confinement of the UCH II region.

4.6. Filling Factor and CS Abundance

The constant density volume filling factor was calculated by taking the ratio of the constant density virial mass ($p = 0$) to the mass calculated from the volume density. The volume density was taken to be the best-fit density from the LVG models, $n_{\rm lvg}$, using multiple transitions of CS and C^{34}S (Paper II),

$$f_v(p = 0) = \frac{M_{\rm vir}(R_{\rm CS}; p = 0)}{(4/3)\pi \mu m_{\rm H} n_{\rm lvg} R_{\rm CS}^3}$$

$$\approx 0.042 \frac{(M_{\rm vir}/1.0 \times 10^4 \ M_\odot)}{(n_{\rm lvg}/1.0 \times 10^6 \ {\rm cm}^{-3})(R_{\rm CS}/1 \ {\rm pc})^3} \ . \quad (11)$$

The average filling factor is 0.46 ± 0.72 with a median of 0.13 for the subsample of 42 cores for which $n_{\rm lvg}$ was determined. Paper II found an average filling factor of 0.33 ± 0.59, consistent with the mean of our sample. However, $f_v(p = 0)$ underestimates the filling factor when there is a density gradient. The LVG models of Paper II assume a constant density envelope; therefore, $n_{\rm lvg}$ represents an average density that is strongly weighted toward the denser gas. Using the power-law models of Mueller et al. (2002b), the

mean $n_{\rm lvg}$ corresponds to the density at a radius of 7300 ± 5200 AU or about 0.1 times the average $R_{\rm CS}$. Detailed models of sources will allow us to determine f_v more accurately, but this comparison suggests that the average core is not highly clumped in the sense of being mostly empty space with a small volume filling factor of very dense clumps probed by the CS emission.

In a similar way, we can compare the mass calculated from the CS column density with the virial mass to constrain the CS abundance,

$$X({\rm CS}) = \frac{\mu m_{\rm H} N_{\rm lvg} \pi R_{\rm CS}^2}{M_{\rm vir}(R_{\rm CS})}$$

$$\approx 5.75 \times 10^{-10} \frac{(N_{\rm lvg}/1.0 \times 10^{14} \ {\rm cm}^{-2})(R_{\rm CS}/1 \ {\rm pc})^2}{(M_{\rm vir}/1.0 \times 10^4 \ M_\odot)} \ . \quad (12)$$

The column density was determined from the LVG models of multiple transitions of CS lines (Paper II). The resulting median value of $X({\rm CS})$ is 1.1×10^{-9}, with a distribution (Fig. 15g) highly skewed by large abundances in G10.6−0.4 [$X({\rm CS}) = 1.3 \times 10^{-8}$], in W28A2 (1) [$X({\rm CS}) = 1.6 \times 10^{-8}$], and in W51 [$X({\rm CS}) = 3.6 \times 10^{-8}$]. The mean and median abundances are 3 times higher than those found in Paper II.

4.7. Luminosity of CS

The luminosity of CS $J = 5 \rightarrow 4$ emission was calculated from

$$L({\rm CS54}) \approx 1.05 \times 10^{-5} \left(\frac{D}{1 \ {\rm kpc}}\right)^2$$

$$\times \left(\frac{\Omega_{\rm source} + \Omega_{\rm beam}}{\Omega_{\rm beam}}\right) \left(\frac{\int T_R^* dv}{1 \ {\rm K \ km \ s}^{-1}}\right) L_\odot \ , \quad (13)$$

using the deconvolved source size and assuming that the source is described by a Gaussian brightness distribution (Paper II). The average CS(5–4) luminosity is $(5.0 \pm 8.8) \times 10^{-2} \ L_\odot$ for the sample of 57 cores, similar to the average CS(5–4) luminosity from Paper II (4.0×10^{-2}). The distribution of CS luminosities is strongly peaked with a tail of high-luminosity sources (Fig. 15h). The median $L({\rm CS54})$ is $1.9 \times 10^{-2} \ L_\odot$, lower than the average luminosity from Paper II, because our sample has included more of the less luminous cores. The total $L({\rm CS54})$ for our subsample of 57 cores is $2.85 \ L_\odot$.

By estimating the number of star-forming cores emitting CS $J = 5 \rightarrow 4$ we can estimate the total Galactic $L({\rm CS54})$. The latest update to the Arcetri H$_2$O maser catalog (Valdettaro et al. 2001) indicates 410 regions with H$_2$O masers that have *IRAS* colors indicative of star formation. Paper II had a detection rate of 75% toward a subset of that sample. Also correcting for the unobserved portion of the Galaxy in the Arcetri survey, roughly 1/3 of the sky, we find that there are roughly 460 cores detectable in the CS $J = 5 \rightarrow 4$ line in our Galaxy. This number may be an understimate since water masers are variable and some water maser sources may not have been detected in the Arcetri catalog. We add the total luminosity from our subsample to the mean $L({\rm CS54})$ for the remaining CS $J = 5 \rightarrow 4$ emitting clouds ($460 - 57 = 403$) to find a Galactic luminosity, $L_{\rm gal}({\rm CS54})$, of 23 $L_\odot$. If the median $L({\rm CS54})$ is used, $L_{\rm gal}({\rm CS54}) \approx 11 \ L_\odot$. If the detection rate is 100% and the average $L({\rm CS54})$ is used, then

L_{gal}(CS54) has an upper limit of 31 $L_\odot$. Therefore, the total Galactic L(CS54) is likely between 11 and 31 $L_\odot$ with a value most likely near 20 $L_\odot$. Assuming that CS $J = 5 \rightarrow 4$ emission is confined to dense cores within molecular clouds (see Helfer & Blitz 1997), this estimate of the Galactic L(CS54) is probably complete. This is consistent with previous estimates of the Galactic luminosity from Paper II and is well below the CS luminosities of nearby starburst galaxies (see Table 8 in Paper II).

4.8. Star Formation Rate per Unit Mass

The ratio of bolometric luminosity to virial mass is roughly proportional to the star formation rate per unit mass. The bolometric luminosity is calculated from fluxes collected in Table 2 of Mueller et al. (2002b). The average L_{bol}/M_{vir} ratio is 314 $(L/M)_\odot$, ranging from 3 to 2290 $(L/M)_\odot$ for a subsample of 40 cores with sufficient flux information to calculate L_{bol}. This average is somewhat higher than those computed for our subsample with masses from dust emission (136 ± 100) and from the sample of Beuther et al. (2002) (120 ± 90), once similar assumptions about dust opacity are made (Mueller et al. 2002b). We can compare with the values in Paper II after correcting the Paper II virial mass for density gradients and optically thick CS line widths to find $L_{bol}/M_{vir} = 440 \pm 100$ $(L/M)_\odot$. The L_{bol}/M_{vir} ratio was higher for Paper II due to a bias toward the most luminous high-mass star-forming regions.

Sridharan et al. (2002) found that their sample of sources with low radio continuum emission had a systematically lower L_{bol}/M_{vir} than did a sample of regions with UCH II regions (Hunter et al. 2000). They interpreted this difference as an evolutionary effect: the sources without well-developed H II regions were younger and had yet to reach their full luminosity. Our sample provides a good check of this hypothesis because it was chosen without regard for the presence of an H II region. The majority of the cores in the L_{bol}/M_{vir} distribution are associated with H II regions (43%) or UCH II regions (38%). The L_{bol}/M_{vir} ratio for cores with H II regions is higher [$\mu_{1/2} = 258$ $(L/M)_\odot$] than for cores with UCH II regions [$\mu_{1/2} = 166$ $(L/M)_\odot$], and higher still than for cores without any known radio continuum [$\mu_{1/2} = 103$ $(L/M)_\odot$]. The distribution of L/M is plotted in Figure 15i. Thus, our data provide some support for the interpretation by Sridharan et al. (2002), but the difference is not great, the overlap of the three samples is substantial, and we have a small number of cores without radio continuum emission. The L_{bol}/M_{vir} for cores with UCH II regions is 1.6 times that for the sample without, similar to the enhancement of the sample of H II regions studied by Hunter et al. (2000) over that studied by Sridharan et al. (2002), according to the analysis of those samples by Mueller et al. (2002b).

All these ratios are much higher than the L_{bol}/M_{vir} for molecular clouds, as traced by CO generally [0.4 $(L/M)_\odot$; Bronfman et al. 2000] or the enhanced value for molecular clouds with bright H II regions [4 $(L/M)_\odot$; Mooney & Solomon 1988]. The dispersion in this ratio is also less than that for studies using CO, again indicating that the dense cores are the relevant entities for the study of massive star formation. This result agrees with studies of HCN toward galaxies that show a tight, linear relation between far-infrared luminosity and luminosity of HCN emission (Solomon, Downes, & Radford 1992; Gao & Solomon
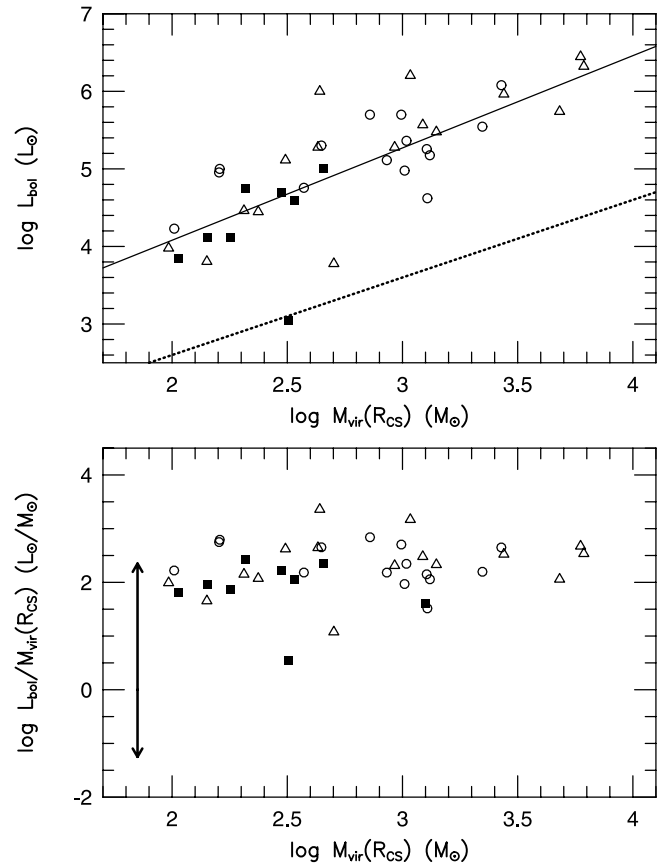

Fig. 21.—Top panel plots L_{bol} vs. M_{vir}, and bottom panel plots L_{bol}/M_{vir} vs. the M_{vir}. Sources with H II regions are plotted as open triangles, sources with UCH II regions are plotted as open circles, and sources without a known UCH II region are plotted as filled squares. The dotted line in the top panel is the relationship derived for CO clumps, while the solid line is a least-squares fit. L_{bol}/M_{vir} is proportional to the star formation rate per unit mass. The range of L_{bol}/M_{vir} for CO clumps is shown as a double arrow at the left of the bottom panel. The dispersion observed toward CS cores is roughly 6 times smaller than the equivalent relationship for CO clumps (Evans 1991).

2002). Those authors argue that the global star formation rate per unit mass depends on the fraction of molecular gas in a dense phase. We see the same trend in dense cores in our Galaxy, suggesting that studies of these dense cores may provide information on conditions in galaxies with intense star formation.

A strong correlation ($r = 0.75$) between bolometric luminosity and virial mass is observed for our sample of cores (Fig. 21), $\log L_{bol} = (1.70 \pm 0.83) + (1.19 \pm 0.11) \log M_{vir}$. The corresponding trend for CO clumps is shown as a dashed line with slightly flatter slope. There is no trend in L_{bol}/M_{vir} versus M_{vir} over 2 orders of magnitude in virial mass (Fig. 21). This result is very similar to the lack of correlation seen for CO clumps over 4 orders of magnitude in mass (see Evans 1991), except that the dispersion in L_{bol}/M_{vir} for the CS cores in this survey is a factor of 6 smaller than for CO clumps. In the dense cores within molecular clouds, the star formation rate per unit mass does not depend on the mass of the core.

Because the luminosity is strongly affected by the most massive star [$L \propto M_\star^\alpha$ with $\alpha \sim 3.5$ up to $M_\star \sim 60$ $M_\odot$ (Scalo 1986)], the linear relation between luminosity and mass and modest dispersion about the relation suggests that

the mass of the most massive star is closely related to the mass of the core, with a relation that approximates $M_\star(\mathrm{max}) \sim M_{\mathrm{vir}}^{1/3.5}$. Because the mass of the most massive star must be subject to strong statistical fluctuations, the dispersion in $L_{\mathrm{bol}}/M_{\mathrm{vir}}$ is surprisingly small; a factor of 2 change in the mass of the most massive star will cause a change of a factor of 11 in luminosity about the dispersion that we observe. Sridharan et al. (2002) come to a similar conclusion based on their sample of sources without UCH II regions.

4.9. Galactic Trends

The core size, line width, virial mass, surface density, CS abundance, and luminosity-to-mass ratio are plotted versus Galactic radius in Figure 22. The large spike in core sizes near $D_g = 10$ kpc is due to the massive cores observed toward the W49 and G32.80+0.20 star-forming regions. There is little evidence for a trend in core size ($r = -0.01$) or line width ($r = -0.14$). There may be weak anticorrelations of surface density ($r = -0.20$), virial mass ($r = -0.26$), and
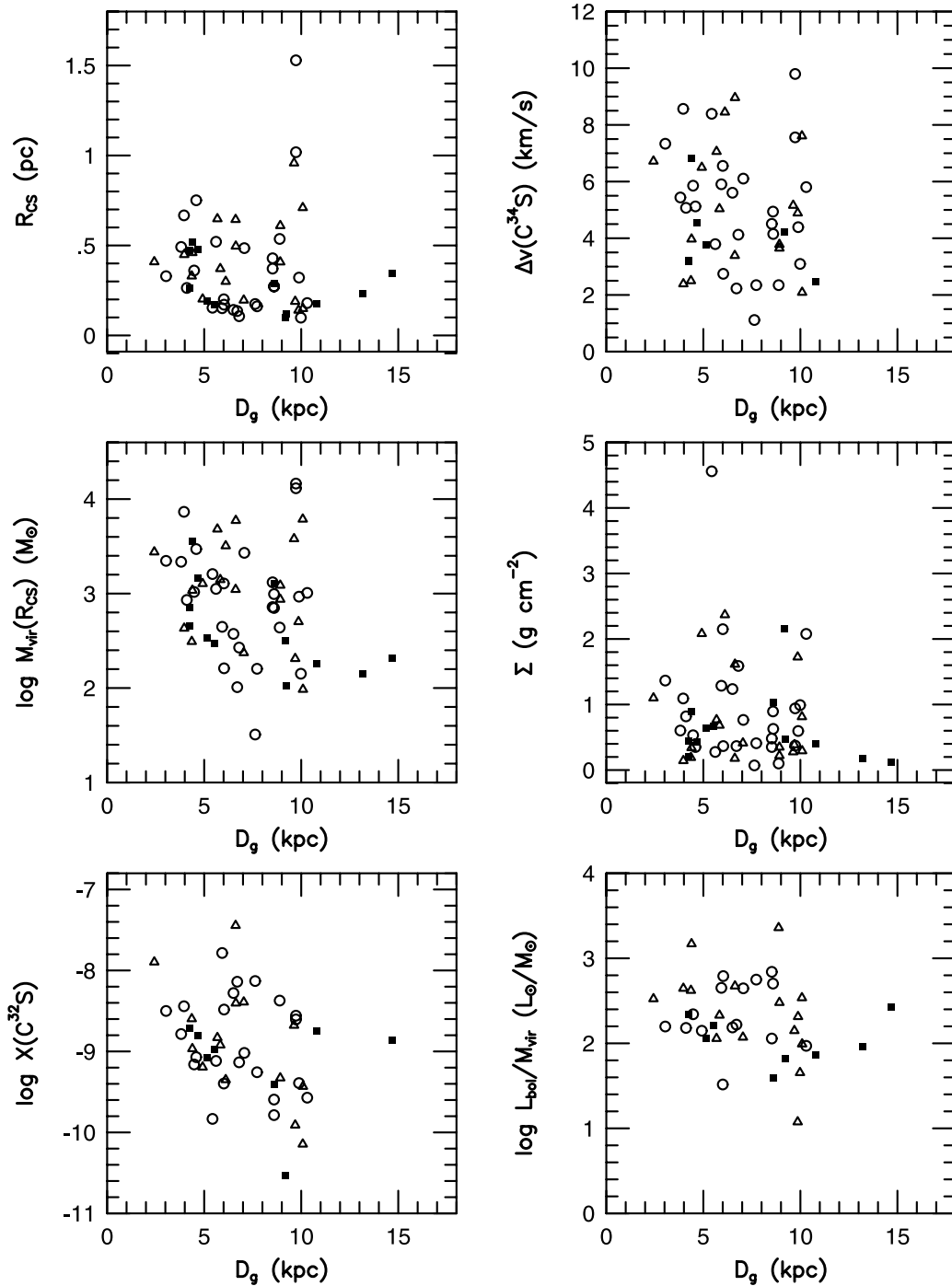
Fig. 22.—Plot of R_{CS}, $\Delta v(\mathrm{C}^{34}\mathrm{S})$, M_{vir}, Σ, $X(\mathrm{CS})$, and $L_{\mathrm{bol}}/M_{\mathrm{vir}}$ vs. galactocentric distance. Sources with H II regions are plotted as open triangles, sources with UCH II regions are plotted as open circles, and sources without a known UCH II region are plotted as filled squares. Only the CS abundance shows a weak correlation with galactocentric distance.

luminosity-to-mass ratio ($r = -0.26$) with D_g. The strongest, but still weak, correlation is between log CS abundance and galactocentric radius ($r = -0.32$). These results mostly agree with previous CS surveys, which found few trends with galactocentric distance (e.g., Zinchenko 1995; Zinchenko et al. 1998). In particular, Zinchenko et al. (1998) also noted a weak correlation ($r = -0.35$) of L/M with D_g.

Zinchenko et al. (1998) found that the most significant correlation in their sample was a decrease of mean density with D_g. Their mean densities were obtained from the CS column densities, determined from the CS $J = 2$–1 line, assuming an abundance of CS that is constant with D_g. In contrast, we find no evidence for a decrease in the density determined from the LVG modeling in Paper II with D_g ($r = -0.03$). We do see an anticorrelation in CS abundance with D_g at about the same level of significance as the correlation Zinchenko et al. found in mean density. A decrease in abundance could have introduced an artificial decrease in their mean densities because they assumed a constant abundance. A decrease in abundance of CS could be caused by many factors, but a simple explanation would be a Galactic gradient in sulfur abundance, as has been found by Rudolph et al. (1997).

5. CONCLUSIONS

We have mapped 63 high-mass star-forming cores associated with water masers in CS $J = 5 \rightarrow 4$. The source size, aspect ratio, virial mass, surface density, CS(5–4) luminosity, and L_{bol}/M_{vir} ratio were calculated. A statistical summary of all calculated quantities is shown in Table 6. Typically, smaller average sizes and masses are found compared with results from Paper II due to the inclusion of weaker sources. Our main conclusions are as follows.

1. A strong correlation is observed between the integrated intensity of the CS $J = 5 \rightarrow 4$ line and continuum flux observed at 350 μm (Mueller et al. 2002b), indicating that high-J CS emission is an excellent tracer of dense gas in high-mass star-forming cores.

2. The median size is 0.32 pc. While a power-law density profile does not have a characteristic size, the median FWHM size is comparable to the core size from dust emission (R_n) determined by Mueller et al. (2002b), based on setting the outer radius at the point where the density drops to 10^4 cm^{-3}.

3. Most of the core aspect ratios are consistent with spherical symmetry. No trend is seen in aspect ratio with p, the exponent in the power-law density distribution.

4. A weak trend between deconvolved source size and p is observed, as expected for power-law density profiles.

5. There is a very weak correlation between line width and size that is consistent with $\Delta v \propto R_{CS}^{0.3}$. The line widths of the cores in this sample are much larger than would be predicted from the Caselli & Myers size–line width relation (1995), indicative of high turbulence.

6. The median virial mass is 920 $M_\odot$ after corrections using C^{34}S line width and p. On average, the virial mass is 2 to 3 times larger than the mass calculated from 350 μm dust emission toward the same region.

7. Sources without known radio continuum emission have median CS intensities, sizes, and masses that are smaller than sources associated with UCH II, CH II, or H II regions.

8. The cumulative mass spectrum is steeper ($\Gamma = -0.9 \pm 0.2$) than studies of molecular clouds as a whole and clumps within those clouds. It is flatter than the Salpeter IMF, but similar to that of the IMF of OB associations and the distribution of total masses of stars in OB associations.

9. The median pressure of the sample is 1.5×10^8 K cm^{-3}. The high pressure may ameliorate the long-standing lifetime problem for confinement of ultracompact H II regions.

10. The L_{bol}/M_{vir} ratio is about 2 orders of magnitude higher than estimates made from tracers of lower density gas (CO) and has a smaller dispersion, indicating that dense cores traced by submillimeter continuum and high-J CS emission are the relevant entities for assessing the star formation rate per unit mass. The L_{bol}/M_{vir} ratio is 1.6 times larger for cores with UCH II regions compared with cores without UCH II regions.

11. A strong correlation is observed between luminosity and virial mass. This result combined with the low dispersion in L_{bol}/M_{vir} indicates that the mass of the most massive star is likely related to the mass of the core.

12. No trends in size, mass, or L_{bol}/M_{vir} with galactocentric radius are apparent. A weak decrease in CS abundance with galactocentric distance is observed.

REFERENCES

Anglada, G., Estalella, R., Pastor, J., Rodríguez, & Haschick, A. D. 1996, ApJ, 463, 205
Bertoldi, F., & McKee, C. F. 1992, ApJ, 395, 140
Beuther, H., Schilke, P., Menten, K. M., Motte, F., Sridharan, T. K., & Wyrowski, F. 2002, ApJ, 566, 945
Blitz, L. 1993, in Protostars & Planets III, ed. E. H. Levy & J. I. Lunine (Tucson: Univ. Arizona Press), 125
Blitz, L., Fich, M., & Stark, A. A. 1982, ApJS, 49, 183
Bonnell, I. A., Bate, M. R., Clarke, C. J., & Pringle, J. E. 1997, MNRAS, 285, 201
Bonnell, I. A., Bate, M. R., & Zinnecker, H. 1998, MNRAS, 298, 93
Brand, J., & Blitz, L. 1993, A&A, 275, 67
Brand, J., & Wouterloot, J. G. A. 1995, A&A, 303, 851
Brand, J., Wouterloot, J. G. A., Rudolph, A. L., & de Geus, E. J. 2001, A&A, 377, 644
Braz, M. A., & Epchtein, N. 1983, A&A, 54, 167
Bronfman, L., Casassus, S., May, J., & Nyman, L.-Å. 2000, A&A, 358, 521
Bronfman, L., Nyman, L.-A., & May, J. 1996, A&AS, 115, 81
Carpenter, J. M. 2000, AJ, 120, 3139
Caselli, P., & Myers, P. C. 1995, ApJ, 446, 665
Cesaroni, R., Palagi, F., Felli, M., Catarzi, M., Comoretto, G., DiFranco, S., Giovanardi, G., & Palla, F. 1988, A&AS, 76, 445
Chini, R., Kreysa, E., Mezger, P. G., & Gemuend, H. -P. 1986, A&A, 154, L8
Churchwell, E., Wolfire, M. G., & Wood, D. O. S. 1990, ApJ, 354, 247
Conti, P. S., & Blum, R. D. 2002, ApJ, 564, 827
De Pree, C. G., Rodriguez, L. F., & Goss, W. M. 1995, Rev. Mexicana Astron. Astrofis., 31, 39
Dickel, H. R., Williams, J. A., Upham, D. E., Welch, W. J., Wright, M. C. H., Wilson, T. L., & Mauersberger, R. 1999, ApJS, 125, 413

Downes, D., Wilson, T. L., Bieging, J., & Wink, J. 1980, A&A, 91, 186
Dreher, J. W., Johnston, K. J., Welch, W. J., & Walker, R. C. 1984, ApJ, 283, 632
Evans II, N. J. 1991, in ASP Conf. Ser. 20, Frontiers of Stellar Evolution McDonald Observatory 50th Anniversary, ed. D. L. Lambert (San Francisco: ASP), 45
Evans II, N. J., Shirley, Y. L., Mueller, K. E., & Knez, C. 2002, in ASP Conf. Ser. 267, Hot Star Workshop III: The Earliest Phases of Massive Star Birth, ed. P. A. Crowther (San Francisco: ASP), 17
Fich, M. Blitz, L., & Stark, A. A. 1989, ApJ, 342, 272
Gao, Y., & Solomon, P. M. 2002, ApJ, submitted
Genzel, R., & Downes, D. 1977, A&AS, 30, 145
Gregersen, E. M., Evans II, N. J., Zhou, S., & Choi, M. 1997, ApJ, 484, 256
Harris, S., & Wynn-Williams, C. G. 1976, MNRAS, 174, 649
Hatchell, J., Fuller, G. A., Millar, T. J., Thompson, M. A., & MacDonald, G. H. 2000, A&A, 357, 637
Helfer, T. T., & Blitz, L. 1997, ApJ, 478, 233
Hofner, P., Kurtz, S., Churchwell, E., Walmsley, C. M., & Cesaroni, R. 1996, ApJ, 460, 359
Hunter, T. R., Benford, D. J., & Serabyn, E. 1996, PASP, 108, 1042
Hunter, T. R., Churchwell, E., Watson, C., Cox, P., Benford, D. J., & Roelfsema, P. R. 2000, AJ, 119, 2711
Jaffe, D. T., Hildebrand, R. H., Keene, J., Harper, D. A., Lowenstein, R. F., & Moran, J. M. 1984, ApJ, 281, 225
Jijina, J., Myers, P. C., & Adams, F. C. 1999, ApJS, 125, 161
Johnstone, D., Wilson, C. D., Moriarty-Schieven, G., Joncas, G., Smith, G., Gregersen, E., & Fich, M. 2000, ApJ, 545, 327
Juvela, M. 1996, A&AS, 118, 191
Klessen, R. 2001, ApJ, 556, 837
Knez, C., Shirley, Y. L., Evans II, N. J., & Mueller, K. E. 2002, in ASP Conf. Ser. 267, Hot Star Workshop III: The Earliest Phases of Massive Star Birth, ed. P. A. Crowther (San Francisco: ASP), 375
Kooi, J. 1998, CSO Tech. Memo., 1998 July
Kooi, J., Chan, M., Phillips, T. G., Bumble, B., & Leduc, H. G. 1992, IEEE Trans. Microwave Theory Tech., 40, 812
Kooi, J., Schaffer, P. L., Bumble, B., LeDuc, R., & Phillips, T. G. 1998, Proc. SPIE, 3357, 22
Kramer, C., Stutzki, J., Rohrig, R., & Corneliussen, U. 1998, A&A, 329, 249
Kurtz, S. 2002, in ASP Conf. Ser. 267, Hot Star Workshop III: The Earliest Phases of Massive Star Birth, ed. P. A. Crowther (San Francisco: ASP), 81
Kurtz, S., Cesaroni, R., Churchwell, E., Hofner, P., & Walmsley, C. M. 2000, in Protostars & Planets IV, ed. V. Mannings, A. P. Boss, & S. S. Russell (Tucson: Univ. Arizona Press), 299
Kurtz, S., Churchwell, E., & Wood, D. O. S. 1994, ApJS, 91, 659
Kurtz, S., & Franco, J. 2002, Rev. Mexicana Astron. Astrofis. Ser. Conf., 12, 16
Kutner, M. L., & Ulich, B. L. 1981, ApJ, 250, 341
Lee, J.-E., Young, C. H., Shirley, Y. L., Mueller, K. E., & Evans II, N. J. 2002, in ASP Conf. Ser. 267, Hot Star Workshop III: The Earliest Phases of Massive Star Birth, ed. P. A. Crowther (San Francisco: ASP), 377
Mangum, J. G., Emerson, D. T., & Greisen, E. W. 2000, in ASP Conf. Ser. 217, Imaging at Radio through Submillimeter Wavelengths (San Francisco: ASP), 179
Mardones, D., Myers, P. C., Tafalla, M., Wilner, D. J., Bachiller, R., & Garay, G. 1997, ApJ, 489, 719
Massey, P., Johnson, K. E., & Degioa-Eastwood, K. 1995, ApJ, 454, 151
Matzner, C. D. 2002, ApJ, 566, 302
McKee, C. F., & Tan, J. C. 2002, Nature, 416, 59
———. 2003, ApJ, 585, 850
McKee, C. F., & Williams, J. P. 1997, ApJ, 476, 144
Meyer, M. R., Adams, F. C., Hillenbrand, L. A., Carpenter, J. M., & Larson, R. B. 2000, in Protostars and Planets IV, ed. V. Mannings, A. P. Boss, & S. S. Russell, (Tucson: Univ. Arizona Press), 121

Mooney, T. J., & Solomon, P. M. 1988, ApJ, 334, 51
Motte, F., André, P., & Neri, R. 1998, A&A, 336, 150
Mueller, K. E., Shirley, Y. L., Evans II, N. J., & Jacobson, H. R. 2002a, in ASP Conf. Ser. 267, Hot Star Workshop III: The Earliest Phases of Massive Star Birth, ed. P. A. Crowther (San Francisco: ASP), 395
———. 2002b, ApJS, 143, 469
Olmi, L., & Cesaroni, R. 1999, A&A, 352, 266
Ossenkopf, V., & Henning, T. 1994, A&A, 291, 943
Penzias, A. A., & Burrus, C. A. 1973, ARA&A, 11, 51
Phillips, T. G., Huggins, P. J., Wannier, P. G., & Scoville, N. Z. 1979, ApJ, 231, 720
Pirogov, L., Zinchencko, I., Caselli, P., Johansson, L. E. B., & Myers, P. C. 2003, A&A, 405, 639
Plume, R., Jaffe, D. T., & Evans II, N. J. 1992, ApJS, 78, 505 (Paper I)
Plume, R., Jaffe, D. T., Evans II, N. J., Martin-Pintado, J., Gomez-Gonzalez, J. 1997, ApJ, 476, 730 (Paper II)
Press, W. H., Teukolsky, S. A., Vetterling, W. T., & Flannery, B. P. 1992, Numerical Recipes in C (2d ed.; Cambridge: Cambridge Univ. Press)
Rudolph, A. L., Simpson, J. P., Haas, M. R., Erickson, E. F., & Fich, M. 1997, ApJ, 489, 94
Salpeter, E. E. 1955, ApJ, 121, 161
Scalo, J. M. 1986, Fundam. Cosmic Phys., 11, 1
———. 1998, in ASP Conf. Ser. 142, The Stellar Initial Mass Function, ed. G. Gilmore & D. Howell (San Francisco: ASP), 201
Scott, P. F. 1978, MNRAS, 183, 435
Scoville, N. Z., & Sanders, D. B. 1987, in Interstellar Processes, ed. D. J. Hollenbach, & H. A. Thronson, Jr. (Dordrecht: Kluwer), 21
Serabyn, E., Güsten, R., & Schulz, A. 1993, ApJ, 413, 571
Shirley, Y. L., Evans II, N. J., & Rawlings, J. M. C. 2000, ApJS, 131, 249
———. 2002a, ApJ, 575, 337
Shirley, Y. L., Evans II, N. J., Mueller, K. E., Knez, C., & Jaffe, D. T. 2002b, in ASP Conf. Ser. 267, Hot Star Workshop III: The Earliest Phases of Massive Star Birth, ed. P. A. Crowther (San Francisco: ASP), 417
Shu, F. H., Adams, F. C., & Lizano, S. 1987, ARA&A, 25, 23
Solomon, P. M., Downes, D., & Radford, S. 1992, ApJ, 387, L55
Solomon, P. M., Rivolo, A. R., Barret, J., & Yahil, A. 1987, ApJ, 319, 370
Sridharan, T. K., Beuther, H., Schilke, P., Menten, K. M., & Wyrowski, F. 2002, ApJ, 566, 931
Terebey, S., Chandler, C., & André, P. 1993, ApJ, 414, 579
Testi, L., & Sargent, A. I. 1998, ApJ, 508, L91
Turner, B. E., & Matthews, H. E. 1984, ApJ, 277, 164
Valdettaro, R., et al. 2001, A&A, 368, 845
Val'tts, I. E., Ellingsen, S. P., Slysh, V. I., Kalenskii, S. V., Otrupcek, R., & Larionov, G. M. 2000, MNRAS, 317, 315
van der Tak, F. F. S., van Dishoeck, E. F., Evans II, N. J., & Blake, G. A. 2000, ApJ, 537, 283
Williams, J. P., Blitz, L., & McKee, C. F. 2000, in Protostars & Planets IV, ed. V. Mannings, A. P. Boss, & S. S. Russell (Tucson: Univ. Arizona Press), 97
Wilner, D. J., Welch, W. J., & Forster, J. R. 1995, ApJ, 449, L73
Wilson, T. L., & Rood, R. 1994, ARA&A, 32, 191
Wink, J. E., Altenhoff, W. J., & Mezger, P. G. 1982, A&A, 108, 227
Wood, D. O. S., & Churchwell, E. 1989a, ApJ, 340, 265
———. 1989b, ApJS, 69, 831
Xie, T., Mundy, L. G., Vogel, S. N., & Hofner, P. 1996, ApJ, 473, L131
Young, C. H., Shirley, Y. L., Evans II, N. J., & Rawlings, J. M. C. 2003, ApJS, 145, 111
Zhou, S., Evans II, N. J., & Wang, Y. 1996, ApJ, 466, 296
Zinchenko, I. 1995, A&A, 303, 554
Zinchenko, I., Forsstroem, V., Lapinov, A., & Mattila, K. 1994, A&A, 288, 601
Zinchenko, I., Mattila, K., & Toriseva, M. 1995, A&AS, 111, 95
Zinchenko, I., Pirogov, L., & Toriseva, M. 1998, A&AS, 133, 337